EXPLORATION OF SOLID HELIUM 4 AT MULTIPLE FREQUENCIES USING A COMPOUND TORSIONAL OSCILLATOR

By MICHAEL C KEIDERLING

A Dissertation submitted to the

Graduate School-New Brunswick

Rutgers, the State University of New Jersey

In partial fulfillment of the requirements

For the degree of

Doctor of Philosophy

Graduate Program in Physics

Written under the direction of

Prof. Harry Kojima

And approved by

_____

_____

_____

_____

_____

New Brunswick, New Jersey

October 2015

ABSTRACT OF THE DISSERTATION

Exploration of Solid Helium 4 at Multiple Frequencies Using a Compound Torsional Oscillator

By Michael Keiderling

Dissertation Director: Prof. Harry Kojima

Apparent but controversial evidence of supersolidity, a coexistence of crystalline and superfluid states, was observed in 2004. Samples of solid ^{4}He were grown, in a chamber, inside a torsion oscillator (TO). The samples showed evidence of apparent decoupling from their container in the form of a resonant frequency increase of the TO as the temperature was lowered. We have developed a Compound torsion oscillator (CTO), with two resonant modes, that allows us to observe a single solid helium sample at two frequencies simultaneously. This thesis will cover the first comprehensive study on the frequency dependence of the apparent supersolid effect. This includes a study of the effect of varying ^{3}He concentrations (x_3) on the frequency dependence. Additionally a study on how changes in x_3 affect the dissipation, which previous studies of x_3 dependence have not explored. Also studied is how varying x_3 affected the hysteresis first observed by Aoki et al. The CTO has allowed the exploration of the amplitude dependent effects in new ways. By exciting the sample at both frequencies simultaneously and

varying the driving amplitude of one mode one can see how excitations at one mode affect what is observed at the other.

The studies of the effects of varying x_3 show results that are consistent with the dislocation movement model proposed by Iwasa. The collected data was not consistent with the simple supersolid model initially proposed. The studies of hysteresis show that the onset of hysteresis was dependent on x_3 but was not frequency dependent. This lends credit to the hysteresis being due to the pinning and unpinning of ^{3}He impurities. The studies of the effect of amplitude dependent effects show an asymmetry between the two frequencies. The higher frequency has a larger effect on the lower frequency than the lower frequency has on the higher. This is also inconsistent with the initial simple supersolid model.

Dedication

To my friends and family, thank you for helping me keep going.

Table of Contents

Lists of Tables

List of Figures

Notation

Chapter 1: Introduction

1: Theoretical Motivation

The theoretical possibility of a new phase of solid helium with superfluid properties or a supersolid phase was introduced in 1969 by Andreev and Liftshits [1] as well as by Chester [2]. Due to the high zero point motion of helium, it was proposed that solid crystal helium could contain mobile vacancies at 0K. The vacancies would form a fluid of bosons and thus could form a Bose-Einstein condensate and a superfluid state. This would manifest itself in the form of a crystalline solid with superfluid properties. Experiments were carried out to search for this unusual state of matter. [3]

2: Early Experiments

A supersolid would have the properties of a superfluid, including the ability to flow through channels that are too narrow for the normal fluid to flow through, without dissipation due to viscous resistance. Such channels are referred to as a superleak as they allow only superfluid to leak through. Several experiments to observe these supersolid phenomena were performed, the first of which was performed by Andreev et al. in 1969. [4] This experiment was based on the idea that supersolid helium would be able to flow around solid objects, allowing them to move without dissipation within the supersolid. Andreev et al. [4] embedded a solid iron ball near the top of a cylinder of solid helium and attempted to cool though the supersolid transition after which it was expected that the ball would move downwards due to the force of gravity as the helium flowed around it. No movement, however, was observed.

Armstrong, Helmy and Greenberg [5] searched for a change in the thermal conductivity of hcp ^{4}He that could be interpreted as an enhanced heat flow caused by a supersolid phase. To measure thermal conductivity (k), Armstrong et al. created a thermal gradient over the length of a cylindrical sample of solid ^{4}He by applying a known input of heat. By measuring this gradient it is possible to calculate the thermal conductivity. The thermal conductivity of polycrystalline samples of ^{4}He grown at a constant volume was measured over a temperature range of 25mk< T < 500mK. The $k \propto T^3$ dependence observed is explained by the Poiseuille flow of phonons. No deviations indicating a supersolid state were observed for the temperatures measured.

Leggett [6] suggested that it would be possible to observe the supersolid phase by using a torsional oscillator (TO), containing a solid helium sample in the torsion bob. As the moment of inertia of the sample would change if a portion of the sample became superfluid and decoupled from the container. This change in moment of inertia due to this decoupling was coined Non-Classical Rotational Inertia (NCRI). The size of the NCRI is usually expressed via the Non-Classical Rotational Inertia fraction (NCRIf) which is the portion of the rotational inertia that is decoupled. This would cause a decrease in the resonance period of a torsion oscillator. Bishop, Paalanen and Reppy [7] carried out a TO experiment with a spherical sample of hcp ^{4}He with a ^{3}He impurity concentration (x_3) of 411 ppm and measured the resonance frequency from 2K to 25 mK. No change in resonance frequency was observed within an accuracy of 5 parts in 10^6. This appeared to indicate that a supersolid state, if it did exist, had a NCRIf less than 5×10^{-6} of sample. However, the ^{3}He concentration in the sample was much larger than the 0.3 ppm in commercially available helium gas.

Ho, Bindless and Goodkind [8, 9] measured ultrasound propagation in solid ^{4}He and analyzed the results in terms of the properties of elementary excitations and Bose-Einstein condensation. They measured the attenuation and speed of ultrasonic pulses in a solid ^{4}He sample with 14ppm< x_3 <30ppm ^{3}He impurities. They observed a peak in ultrasound attenuation near 165 mK along with an increase in sound velocity in a sample with x_3=27.5 ppm. They interpreted this anomaly as evidence of a continuous phase transition in hcp solid ^{4}He as would be expected if there were a supersolid phase caused by Bose-Einstein condensation of vacancies.

3: Kim and Chan Experiment

It was thought that the supersolid state would result from the formation of a Bose-Einstein condensate by vacancies within solid helium. Thus, Kim and Chan searched for the supersolid state in solid helium grown in the 7 nm pores of vycor glass which would promote production of vacancies [10, 11]. Measurements were made using a torsion oscillator containing a solid disc of vycor glass in which solid ^{4}He, with a 0.3 ppm ^{3}He content, was grown. The resonance period of this torsion oscillator was measured through a temperature range from 25 mK to 1K. This measured period was compared to the period of the empty cell and the period of a cell filed with solid ^{3}He which was not expected to show supersolidity due to its fermionic nature. The experiments were repeated in bulk helium in the form of an annulus 0.63 mm wide 10 mm in diameter and 5 mm high. Kim and Chan observed a decrease in the period of the oscillator during cooling starting at ~200mK and ending at ~30mK. This change in period indicated a maximum NCRIf of 2.5%. Upon repetition with a bulk helium sample similar results

were seen with an NCRIf of ~1%. In addition, this drop in period showed a distinct dependence on the velocity of oscillation and the concentration of ^{3}He impurities in the solid ^{4}He. The size of the decrease in period was reduced by increasing the velocity of oscillation in a manner similar to the critical velocity effect seen in superfluid ^{4}He, though with a lower critical velocity of ~30 μm/s, as compared to the ~0.5 cm/s seen in superfluid liquid helium. The Kim and Chan experiment [11] cannot distinguish whether the critical velocity effect observed is caused by changes in velocity, acceleration or displacement, as measurements were only made at only one frequency. My experiments will address this question by use of our two frequency torsion oscillator.

4: Disorder Dependence/Geometry Dependence

The NCRIf appears to show dependence on disorder. If a sample with a large surface to volume ratio is quench cooled, the formation of solid will be very fast locking in all the disorder generated in the freezing process. Samples, produced in this manner, have shown some very high maximum NCRIf as much as 14%. [12] However, samples that have been annealed removing much of the disorder show small maximum NCRIf, in some cases reduced below the resolution of the measurements. [12]

Chapter 2: Motivation

1: ^{3}He effect

A question that naturally arises is how the torsional oscillator (TO) response is affected by the addition of ^{3}He impurity to the ^{4}He solid samples. It is not clear how such small amounts of impurities at the ppm levels can alter the response of the oscillator with a sample loaded, here after referred to as 'the TO response' unless otherwise noted, so dramatically [10, 13]. The previous studies on the effects of ^{3}He impurities have left many unanswered questions. While Kim et al. [13] did fit their data with a model based on dislocation pinning, they had to make several assumptions such as that $T_{50,}$ the temperature by which half of the period shift has occurred, is the point at which pinning in the dislocation network in hcp ^{4}He becomes dominated by ^{3}He pinning. In addition, they did not address how the dissipation peak changes with increasing x_3. Effects that the frequency of the oscillator has on the dependence of frequency shift and dissipation on x_3 were not explored. The physical mechanism behind altering TO response by ^{3}He impurity was not understood.

These considerations led us to ask several questions. How is dissipation affected by changes in x_3? How is the temperature at the dissipation peak changed, as x_3 is varied? How does increasing x_3 change the frequency shift and dissipation and their frequency dependence? Are the differences between frequencies larger, smaller or the same? Is the hysteresis we observed dependent on x_3? Once we answer some of these questions we will be better able to answer the big question; what ^{3}He is doing to cause such a large change in frequency shift and dissipation in solid ^{4}He? Is the observed frequency shift

caused by the movement of ^{3}He? Is ^{3}He pinning dislocations and changing their movement? Or does ^{3}He somehow change at what temperature superflow can occur? Only with a better understanding of what the effects of ^{3}He concentration are can we answer these questions.

In this thesis I describe measurement of both frequency shift and dissipation at two frequencies simultaneously. By measuring a series of samples over a range of ^{3}He concentrations we can construct a picture of the x_3 dependence of the frequency shift and dissipation at two frequencies. This allows examining not only how the dissipation peak and frequency shift change but also how the frequency dependence changes. In addition, it enables the systematic study of the hysteresis to determine what, if any, dependence it has on x_3.

2: Drive dependence

In the second part of my thesis, I describe measurements on the dependence of frequency shift on the applied drive level. Earlier work by Aoki et al. [14] compared frequency shift measurements at two frequencies on the same sample of solid ^{4}He. This work demonstrated that the critical velocity effect initially seen by Kim and Chan was a function of the velocity of oscillation and not acceleration or displacement. In addition, Aoki et al. [14] were able to observe a hysteresis effect in frequency shift. These experiments measured TO response at one resonance frequency of the compound torsion oscillator (CTO) at a time.

We developed a technique to measure the compound TO response at the two mode frequencies simultaneously. This led us to ask, if we suppress the frequency shift

by driving with one mode frequency, can we measure that suppression with the other? Does it matter which mode frequency we use to suppress and which we use to measure? Does the notion of critical velocity make sense to use for these systems?

The interactions between two frequencies will hopefully give us insight into the underlying mechanism of the velocity dependence. For example, if the suppression is caused by a superfluid critical effect, we should see that both frequencies will measure the same suppression of frequency shift as it does not matter what frequency the critical velocity is generated at, the superfluid decoupling will be reduced for the entire system, and the frequency shift will change for all modes. However, if the suppression is due to some form of dynamic response of the system such as dislocation movement or a glassy state, the two frequencies may be completely independent of each other.

In addition, we wanted to see what effect increasing the ^{3}He concentration would have on the velocity dependence. Would it change dramatically like the temperature dependence or would it be basically unaffected?

Chapter 3: Experimental techniques

1: Torsional Oscillator

1.1: Single Mode Torsional Oscillator

A single frequency torsional oscillator is composed of a torsion rod and a bob. The bob contains the chamber for a solid ^{4}He sample. The total moment of inertia of the bob is the sum of the moment of inertia of the sample and the chamber. A single mode torsion oscillator is analogous to one mass attached to one spring: one mass (with moment of inertia I) attached to one torsion rod (with torsion constant K). The torsional motion is described by the following equation of motion.

$$I\ddot{\theta} = -K\theta - \zeta\dot{\theta} \qquad (1)$$

where θ is the angular displacement and ζ is the damping constant. The system has a natural resonance frequency (ω_0), given by:

$$\omega_0 = \sqrt{\frac{K}{I}} \cdot \sqrt{1 - \zeta^2} \qquad (2)$$

Our torsional oscillators have a very low value of ζ. Thus the resonant frequency can be safely approximated by the ζ=0 limit.

$$\omega_0 = \sqrt{\frac{K}{I}} \qquad (3)$$

When the oscillator is driven sinusoidally, there is peak in response amplitude at the resonant frequency. The width of the peak is a function of the damping and is described by the quality factor (Q) corresponding to the frequency of the center of the

peak, divided by the width of the peak at ½ the maximum energy (1/√2 the max amplitude). In a torsion oscillator,

$$Q = \frac{\sqrt{K\,I}}{\zeta} \tag{4}$$

For high Q values the width of the peak is difficult to measure, so we utilize a ring down technique to find the Q value.

1.2: Ring Down

To determine Q at temperatures below 4.2 K, we measure a ringing down of resonances. The torsion oscillator is initially driven at resonance with amplitude A_0. Then the driving signal is disconnected. The amplitude of the decaying signal is measured with a Tektronix TDS5032B digital oscilloscope. The decay of amplitude A is fit to an exponential, as seen in Figure 1

$$A = A_0 e^{\frac{-t}{\tau}} + c \tag{5}$$

Here A_0 is the initial amplitude, τ is the time constant and c is a residual background signal due to noise. From this we calculate the quality factor

$$Q_i = \tau_i f_i \pi \tag{6}$$

Where τ_i is the time constant of the exponential decays and f_i is the resonance frequency of the excited mode.

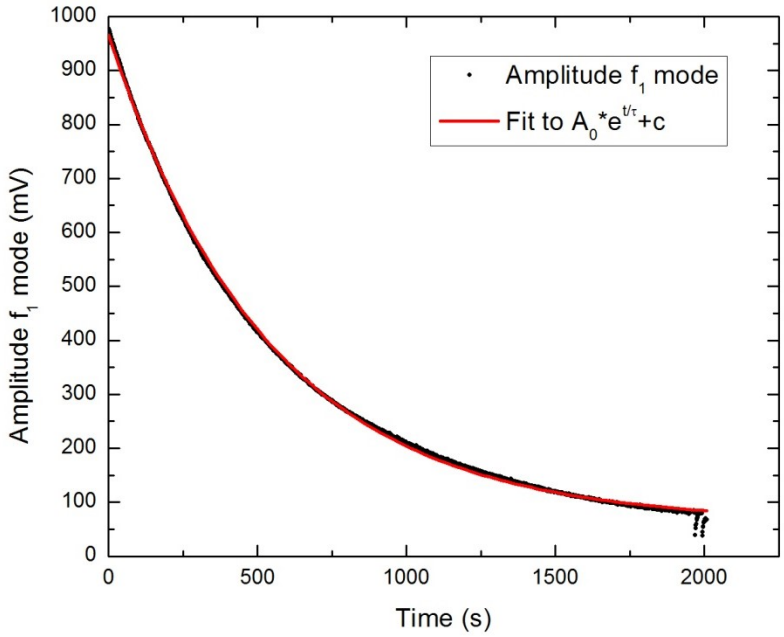

Figure 1, Ring down plot of A_1 vs time: Taken as mode one rings down from a constant drive. The data is fit with the exponential decay $A = A_0 e^{\frac{-t}{\tau}} + c$

This is then used to determine the calibration constant (κ) from amplitude (A) to dissipation Q^{-1}. If the ring down is performed at 250 mK, as most of our ring-downs were, the following formula defines κ.

$$\kappa_i = \frac{Q_i(250mK)}{A_i(250mK)} \qquad (7)$$

Once the calibration constant κ is determined, Q_i is evaluated from the amplitude A_i measured while the TO is driven at resonance.

1.3 Compound Torsional Oscillator

The single mode torsional oscillator is the type most commonly used in supersolid studies. It is, however, very useful and desirable to measure the TO response at two different frequencies. A compound torsional oscillator (CTO) was conceived and

constructed to probe simultaneously, an identical sample under identical conditions, at two different frequencies.

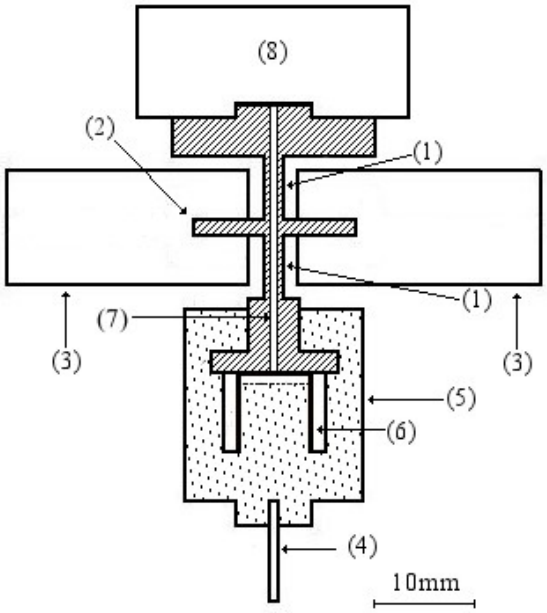

Figure 2, Schematic diagram of the compound torsion oscillator: Showing parts (1) two BeCu torsion rods, (2) upper dummy mass, (3) Al fins for upper electrodes, (4) Al fin for lower electrode, (5) stycast 1266 pressure chamber, (6) annular sample, (7) He fill line, (8) isolation block

A schematic of our system is shown in Figure 2. Our compound TO consists of two torsion rods (Figure 2 (1)) and two bobs one being a "dummy" mass (Figure 2 (2)) and the other being the sample container(Figure 2 (5)). Thus our system has two resonant modes. The motion of our oscillator is described by the following equations of motion.

$$\ddot{\theta}_1 I_1 = -K_1\theta_1 + K_2(\theta_2 - \theta_1) \quad (8)$$

$$\ddot{\theta}_2 I_2 = -K_2(\theta_2 - \theta_1) \quad (9)$$

Here K_1 and K_2 are the torsion constants of the upper and lower rods respectively as shown in Figure 2, I_1 and I_2 are the moments of inertia and θ_1 and θ_2 are the angular

displacements of the upper and lower masses. Assuming harmonic solutions $\theta_1 = \theta_{10}e^{-i\omega t}$ and $\theta_2 = \theta_{20}e^{-i\omega t}$ equations (7) and (8) may be written in matrix form as

$$0 = \begin{bmatrix} -(K_1 + K_2){I_1}^{-1} + \omega^2 & K_2{I_1}^{-1} \\ -K_2{I_2}^{-1} & K_1{I_2}^{-1} + \omega^2 \end{bmatrix} \begin{bmatrix} \theta_1 \\ \theta_2 \end{bmatrix} \tag{10}$$

Allowed frequencies are found by solving $det[matrix] = 0$ leads to the general solution.

$$\begin{aligned} &{\omega_{1,2}}^2 \\ &= \frac{K_2{I_1}^{-1} + K_1{I_1}^{-1} - K_1{I_2}^{-1}}{2} \\ &\pm \frac{\sqrt{2K_1K_2{I_1}^{-2} + {K_2}^2{I_1}^{-1} + {K_1}^2{I_1}^{-2} + {K_1}^2{I_2}^{-2} + 2K_1K_2I_1I_2 + 2{K_1}^2I_1I_2 - 4{K_2}^2}}{2} \end{aligned} \tag{11}$$

While the Eigen values of the above matrix correspond to the frequencies at which the two modes oscillate, the Eigen vectors tell us the relative motion of the upper and lower mass for each mode. This allows us to use the amplitude of motion of one mass to inform us as to the amplitude of motion of the other, allowing us to drive using the upper mass.

Our torsion oscillator consists of two torsion rods (Figure 2 (1)) and two masses (Figure 2 (2, 5)) suspended from an isolation block (Figure 2 (8)). The two beryllium copper rods are machined to identical diameter of 1.9 mm and length of 6.35 mm (Figure 2 (1)). The upper mass is a dummy mass and consists of a disk of beryllium copper 1.5 mm high and 16.2 mm in diameter (Figure 2 (2)). Attached to this disk are two aluminum fins 24.1 mm long, 11.4 mm wide and 1 mm thick (Figure 2 (3)). These are used in conjunction with two electrodes fixed to the isolation block to drive and detect the mechanical oscillations. The lower mass contains the Helium sample; it is a cylinder of Stycast 1266 attached to an upper plate of beryllium copper (Figure 2 (5)). The inside of

this cylinder is the hollow annular sample cell, a cylindrical annulus 8 mm high and 10 mm in diameter and 1 mm thick. Also, attached to the bottom of the lower mass is an aluminum fin 18 mm wide 10 mm tall and 1 mm thick (Figure 2 (4)) which also has a corresponding electrode to detect oscillations.

The torsion rods, the upper mass and the top plate of the sample cell are all machined from a single piece of beryllium copper (Figure 2 (1, 2)). After machining, the beryllium copper part is hardened by being heat treated at 316 °C for 3 hours. This hardens the beryllium copper by allowing the gamma phase to precipitate out. [15] The body of the sample cell is machined from a block of Stycast 1266 (Figure 2 (5)). The aluminum fins are glued to the upper mass using Stycast 2850. The body of the sample cell is attached by placing the lower disc of the torsion rod assembly inside it to form the top of the sample cell and pouring Stycast 1266 on top of this disc so it is entirely encapsulated by the cell body.

This double oscillator has two resonant modes. In the lower mode the two masses move in phase and in the higher mode they move out of phase. We are able to excite and measure as described in the following section both of these resonant modes simultaneously.

1.4 Tracking Frequencies

When a resonant mechanical system is being driven at its resonance frequency, the drive and displacement are $\pi/2$ radians out of phase. The displacement component in-phase with the drive vanishes at resonance. In order to continue driving our system at resonance and to measure the current resonance frequencies, the driving frequency is continually

adjusted to maintain the in-phase component of the displacement at null. The feedback loop we use to do this is shown in Figure 3.

1.4.1 Electronics

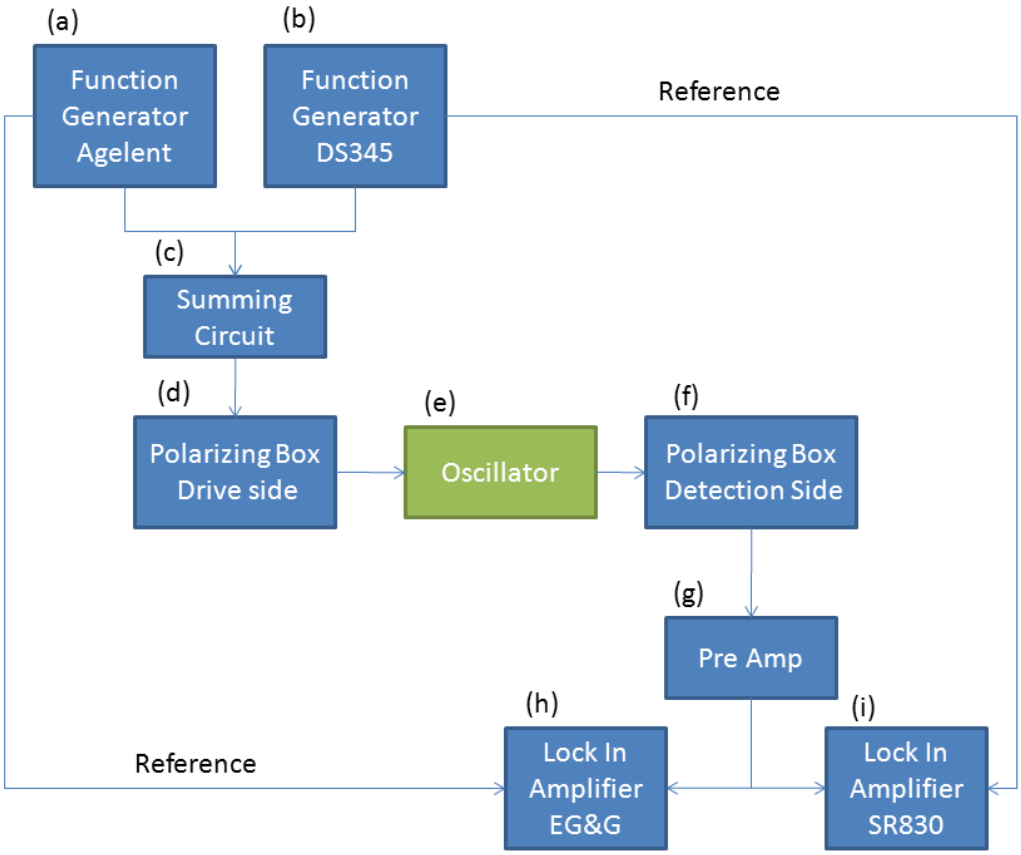

Figure 3, Electronic flow diagram: This diagram show how the various electronics are connected to each other to both drive and measure the resonance of our torsion oscillator.

The oscillator is driven and its movements are measured by two electrodes. They form capacitors with the fins on the torsion oscillator. These electrodes are charged with a constant DC voltage. This is achieved by the polarizing voltage sources which apply DC bias to the electrodes and allow an AC signal to be either applied or measured. On the drive side the sinusoidal driving AC signal is produced by two function generators (Figure 3 (a, b)). The two AC signals are added together by an op amp summing circuit

(Figure 3 (c)) and applied to the polarizing box (Figure 3 (d)). This signal is applied to one of the electrodes in the oscillator (Figure 3 (e)). The other electrode is connected to the detection side of the polarizing box (Figure 3 (f)). The AC signal from this is fed to the preamplifier (Figure 3 (g)). The output of the preamplifier is applied to two lock-in amplifiers (Figure 3 (h, i)) which are able to separate out the components of each individual mode allowing us to simultaneously track the two resonances.

1.4.2 Polarizing box

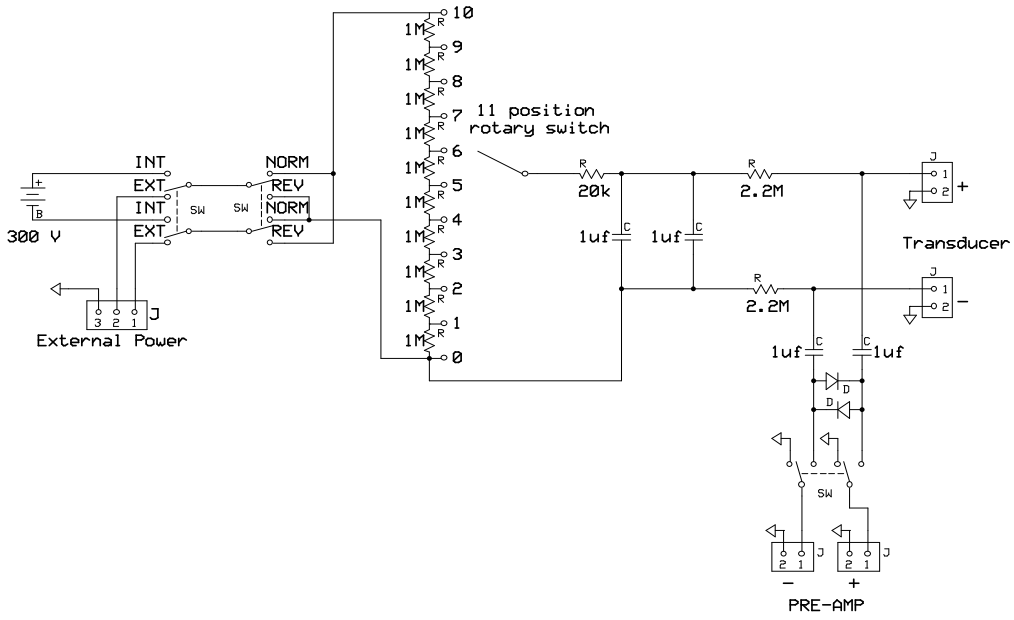

Figure 4, Circuit diagram of the polarizing box: The polarizing box is used to add a DC bias set via a rotary switch to the transducer electrodes. The AC portion of the signal is separated and sent to the pre-amp for detection.

The polarizing box allows us to apply a DC bias on the oscillator electrodes and then either add to it a AC signal from external sources or to separate out any AC component to be amplified and measured the circuit shown in Figure 4. It uses the two large capacitors on the transducer side to let through AC signals while stopping DC

current flow. The other two capacitors allow for a DC bias while preventing a DC current flowing across the electrodes on the oscillator.

1.4.3 Function generator

We use 2 function generators, one for each mode of the oscillator. These are a Stanford research systems DS345 and an Agilent 33220A. Both function generators are set to generate sine waves at desired amplitude. They can create signals that range in amplitude from 10mV to 1V.

1.4.4 Summing circuit

We use an op amp summing circuit to add the signals from the 2 function generators. This generates a signal that is the inverted sum of the output of the function generators. This leads to a drive signal 180 degrees out of phase from the reference signal, something that can be corrected when adjusting the phase of the lock-in amplifiers.

1.4.5 Preamp

After leaving the polarizing box, the signal is amplified by a preamplifier. Much of our data was taken using a Stanford Research Systems model SR 560 low noise voltage pre-amplifier used at a gain of 50-5000 depending on the situation. In most cases a gain of 100 was used. In addition, the internal high and low pass filters were set at 6 dB/octave as well as 10 Hz and 30 kHz respectively. For other experiments, we used Stanford Research Systems model SR570 current preamplifier in an attempt to reduce noise. This amplifier was used with a high pass filter of 6 dB/octave at 10 Hz and a sensitivity of 5 x10 nA/V. This converted a current signal to a voltage signal readable by the lock-in amplifiers.

1.4.6 Lock-In Amplifiers

We use two lock-in amplifiers to measure the signals from the two modes. Lock-in amplifiers measure the magnitude and phase of a signal at a specific reference frequency, independent of signals at other frequencies. In order to correct for lag in electronics, the reference signal is adjusted by a phase of up to 15°. This is done by taking the input signal and multiplying it by a reference sine function at the desired frequency. This produces a DC signal proportional to the in-phase signal strength which can be separated from the AC components of the signal with a low pass filter. By doing this with two reference signals 90° out of phase it is possible to determine the magnitude and phase of the signal and the reference frequency. Using this information we are able to locate and track the resonance peak of our torsion oscillator.

We are able to determine the displacement amplitude using the following calculations. The fin on the cell and the stationary electrode form a capacitor with capacitance C_f as defined below, where A is the area of the electrode, d is the distance from the fin to the electrode, and ε_0 is the permittivity of the vacuum.

$$C_f = \varepsilon_0 \frac{A}{d} \tag{12}$$

Let the applied DC voltage bias be V_{DC}. The coaxial cable leading to the electrodes has a capacitance C_w to ground, where $C_w \gg C_f$. The relationship between the voltage and these two capacitances is shown below. Q is the total charge on the plate and the cable.

$$V_{DC} = \frac{Q}{C_f + C_w} \tag{13}$$

Using these formulas we can find the relationship between small changes in voltage δV and changes in the position of the fins δd.

$$\delta V = \frac{-Q}{\left(C_f + C_w\right)^2}\delta C_f \tag{14}$$

$$\delta V = \frac{V_{dc}}{C_f + C_w}\frac{\varepsilon_0 A}{d^2}\delta d \tag{15}$$

Using only the values we can measure.

$$\delta V = \frac{V_{dc}}{C_f + C_w}\frac{C_f}{\varepsilon_0 A}\delta d \tag{16}$$

What we wish to determine is the amplitude of the oscillation of the fins d_f as a function of the amplitude of AC voltage oscillation Y, which we measure using the lock-in amplifiers. In our set up $\delta V = Y$ so d_f *as* a function of Y can be expressed in equation (17).

$$d_f = \varepsilon_0 A \frac{C_f + C_w}{{C_f}^2}\frac{Y}{V_{dc}} \tag{17}$$

We measure d_f for both the upper and lower fins of our oscillator at the same drive amplitude. The lower fin allows us to directly measure the angular displacement of lower bob containing the sample chamber. By comparing the movement of the upper and lower bobs, we determine how movement measured at the upper bob corresponds to movement of the sample chamber. This allows us to determine a constant which, multiplied by the measured voltage amplitude, gives us the displacement amplitude of the cell at the rim of the sample. This, combined with the frequency of the oscillations, allows us to determine the rim velocity and the rim acceleration.

2: Refrigerator and thermometry

To cool our system we use an Oxford Instruments dilution refrigerator [16] with a base temperature of 5 mK. The temperature is measured with a ruthenium oxide resistance thermometer mounted on the isolator block and four-lead resistance measurement with a Picowatt AVS47 resistance bridge [17] using an excitation of 30 μV. This thermometer was calibrated against the melting pressure curve of ^{3}He [18, 19]. Calibration was carried out using a pressure sensor filled with ^{3}He and cooled along its melting curve. Both the ^{3}He pressure sensor and the RuO resistance thermometer were mounted on the same isolator block of the torsional oscillator.

The temperature is controlled using a heater attached to the mixing chamber of the refrigerator. The heating is controlled by a Perl program that regulates the amount of current based on the difference between the measured temperature from the RuO thermometer and the desired temperature. The temperature can be swept continually at desired rates in a series of steps.

3: Making sample

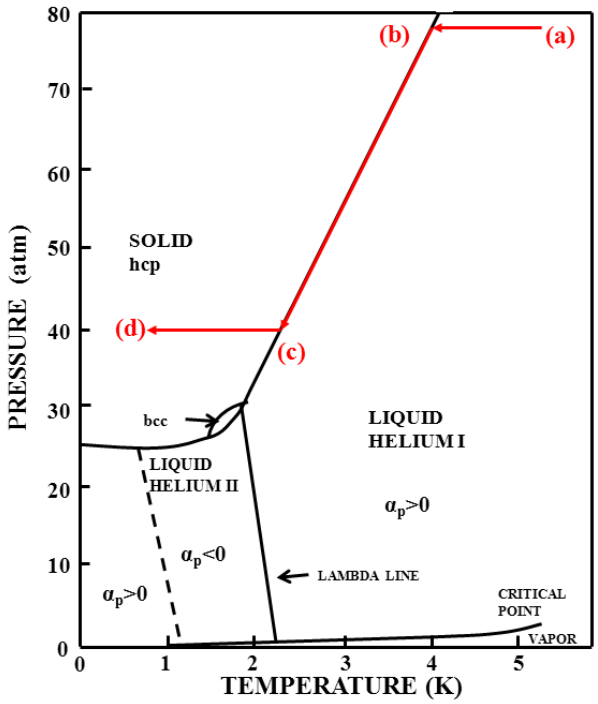

Figure 5, ^{4}He Phase diagram: [20] Showing the cooling path of a ^{4}He sample produced via the blocked capillary method. The sample starts liquid at (a) and cools to the liquid solid transition at (b) where it starts to solidify. The solidification process occurs at fixed volume between (b) and (c) at which point the entire sample is solid it then cooled to (d) where experiments begin.

3.1 Making Solid

Our samples are hcp ^{4}He made using the blocked capillary method. At 4.2 K the cell is filled with liquid at ~80 bar. Then the 1 K pot is filled causing the local temperature to drop to ~1.5 K. This cooling forms a sold block in the fill line near the 1K pot sealing the cell. The cell contains a fixed mass of helium in a fixed volume throughout solid formation leading to large pressure differentials during cooling. To cool the cell after the solid block is formed in the fill line, helium is added to the refrigerator allowing the transmission of heat form the sample cell to the 1K pot. The subsequent cooling of the

system and formation of solid takes ~1 hr and produces a solid sample pressure of less than 40 bar. The cooling curve of the helium sample is illustrated in Figure 5.

3.2 ^{3}He Addition Procedure

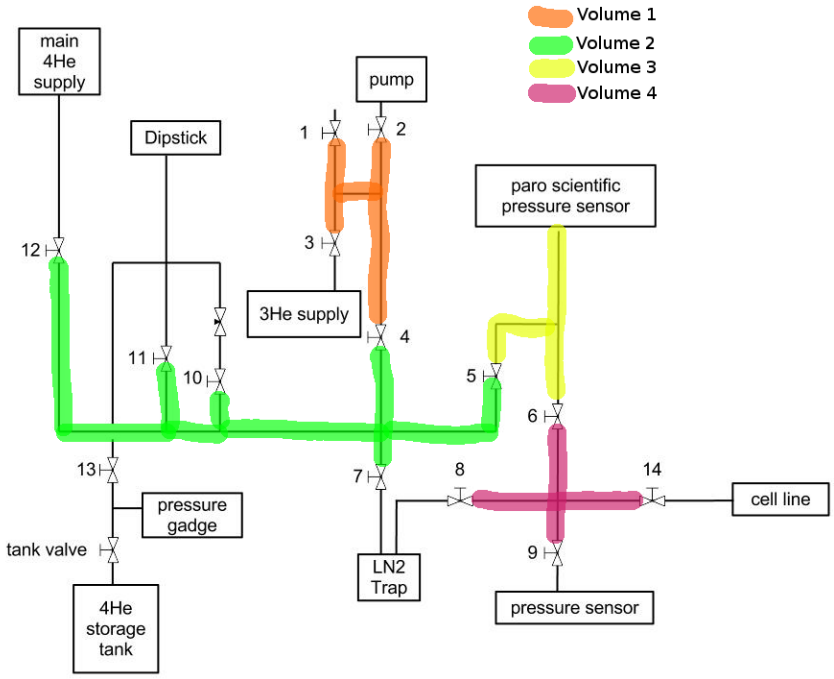

Figure 6, Diagram of the gas handling system: Used to fill the cell and make samples of various ^{3}He concentrations Valves are numbered. Volume 1 is bounded by valves 1, 2, 3 and 4. Volume 2 is bounded by valves 4, 5, 7, 10, 11, and 12. Volume 3 is bounded by valves 5 and 6. Volume 4 is bounded by valves 6, 8, 9 and 14

To achieve a desired concentration of ^{3}He in our samples we first add a known amount of ^{3}He to the cell, using the gas handling system diagramed in Figure 6. The quantity of ^{3}He desired in the cell is less the can be easily added in a single step as the desired x_3 values are in the ppm range. In order to add the small quality of ^{3}He the following procedure is used. Volume 3 in the cell gas handling system is filled with a calculated pressure of ^{3}He. The rest of the system is pumped down. Then the gas is Volume 3 is released in to Volumes 1 and 2 in order to reduce the pressure of ^{3}He in

Volume 3 to desired amount. Volume 3 is sealed and the rest of the system is pumped down. Then Volume 3 is opened to Volume 4 and the cell fill line, placing the desired amount of ^{3}He in to the cell and cell fill line. The cell is sealed off and the rest of the gas handling system is pumped down and flushed with ^{4}He. Then ^{4}He is added to the cell to fill it to the desired pressure, filling the cell with a mixture of ^{3}He and ^{4}He at the desired pressure and ^{3}He concentration.

5: Temperature Sweep

To measure the temperature dependence of frequency and amplitude we start just above 1K as the frequency shift starts below 1K in most cases. Then we cool at a starting rate of 150 mK/hr. As the temperature decreases, we slow down the cooling in a series of steps; for example at 450 mK the rate is changed to 50 mK/hr, at 205 it's reduced to 33 mK/hr, and so on, as seen in Figure 7. This is because at lower temperatures the changes in frequency and amplitude have larger temperature dependence. In addition, at lower temperature the system takes a longer time to relax to equilibrium. Therefore if the temperature is changed too fast the system does not keep up with the temperature changes. While the temperature is changed continually, the system is continually kept on resonance by the tracking software which measures resonance frequency and amplitude.

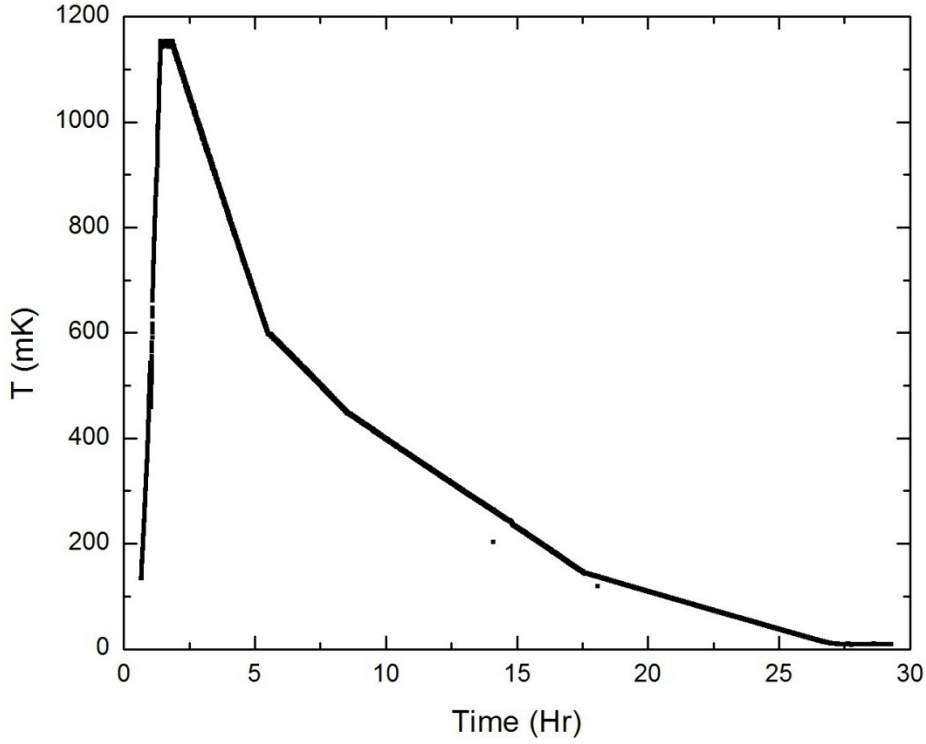

Figure 7, Plot of T vs. time for a T sweep: Showing the series of cooling rates 150 mK/hr. 50 mK/hr, 33 mK/hr and 15 mK/hr starting at 1150 mK, 600 mK, 450 mK, and 125 mK respectively

One potential source of error is that the thermal conductivity of the cell containing helium is larger than that of the empty cell. Thus the cell may cool faster when full than when empty. The temperature is measured at the isolator block, meaning there could be a delay between when the isolator block reaches a temperature and when the cell does. The difference in thermal conductivity between the empty and full cell could lead to a difference in this delay, making comparison of the two difficult. To minimize this effect we use a low rate of temperature change at low temperatures in sweeps.

6: Drive dependence

In order to measure the drive dependent suppression of frequency shift we use the following procedure illustrated in Figure 8. We prepare the initial state of our sample at ~300mK because at this temperature the larger, more rapid, lower temperature part of the frequency shift has ended and we have observed no annealing effect at this temperature. Raising the sample to this temperature between runs clears any hysteresis the sample might have without changing the sample via annealing. First we set the drive of one mode to large amplitude. This mode will be referred to as the driving mode. We set the drive of the other mode to low amplitude to keep that mode in the low velocity limit. This mode will be referred to as the detecting mode. The system is cooled to the desired measurement temperature. Once the temperature has stabilized, the drive amplitude of the driving mode is lowered and then raised in a series of steps, while the drive amplitude of the detecting mode is held constant in the low velocity limit. This procedure reveals the hysteretic nature of the velocity dependence of the frequency shift.

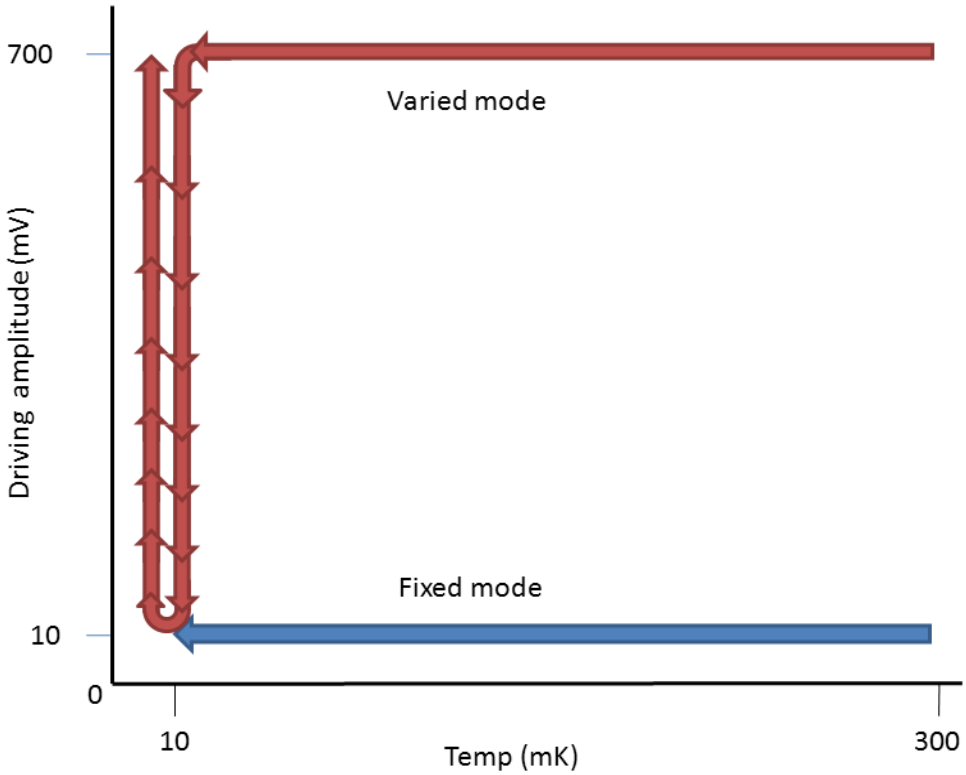

Figure 8, Drive steps: The series of steps used to measure the effect of high drive amplitude on both modes simultaneously. The driving mode is shown in red while the detecting mode is shown in blue and the arrows indicate the series of steps in temperature and drive amplitude taken.

7: Process used to take background data

The resonance frequency and dissipation of the torsion oscillator itself have both temperature and drive dependence. In order to determine what changes in frequency and amplitude are due to the solid ^{4}He sample we measure the empty cell in a manner identical to the way the solid sample will be measured. This gives a background frequency and dissipation that can be subtracted from the values measured with the cell containing a solid sample, enabling us to determine what changes to frequency and dissipation are due to the solid sample.

Chapter 4: Results and Analysis

1: Dependence on ^{3}He Impurity

1.1 Empty Cell Backgrounds

In order to observe how the oscillator behaved independently of and effects from the helium sample, we measured the two resonant modes of our oscillator with the cell empty, as described in Chapter 3 Section 7. This gave us a set of background measurements for the temperature sweeps and drive dependences, as seen in Figure 9. Using this information we were able to remove the effects due to the oscillator from our measurements of the cell containing solid helium sample taken, as described in Chapter 3 Section 5.

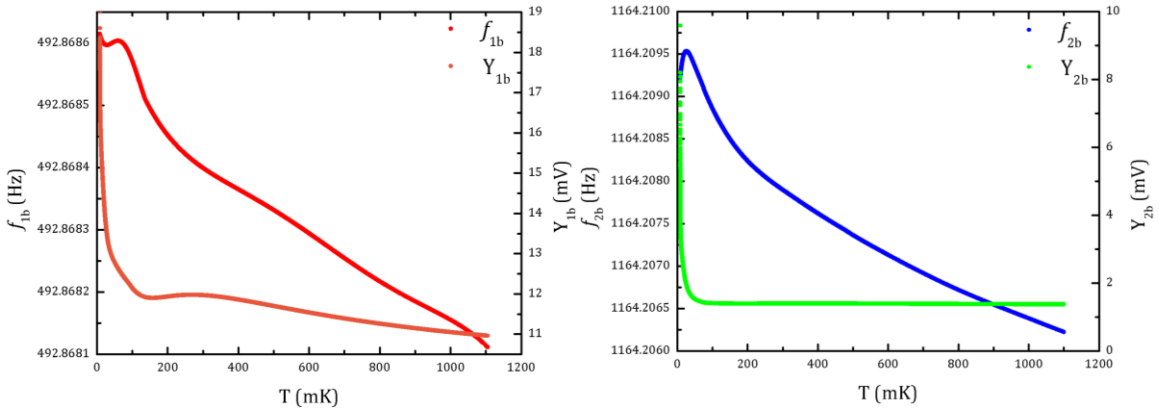

Figure 9, Temperature sweep, with empty cell, of both modes: On the left low drive mode one frequency vs temperature (red) and amplitude vs. Temperature(orange) on the right low drive mode two frequency vs temperature (blue) and amplitude vs. Temperature(green) with empty cell. This data was taken to measure the background effects due to the oscillator alone.

1.2 Procedure For Determining Frequency Shift And Q Inverse

To evaluate frequency shift from the acquired data we first match solid and background frequency data at 0K. The shift required is the loading frequency Δf_i. We then calculate

shift in frequency δf_i by subtracting the shifted background frequency from the solid, as seen in Figure 10. In order to compare the two modes the frequency shift, δf_i is normalized by the frequency at 0K.

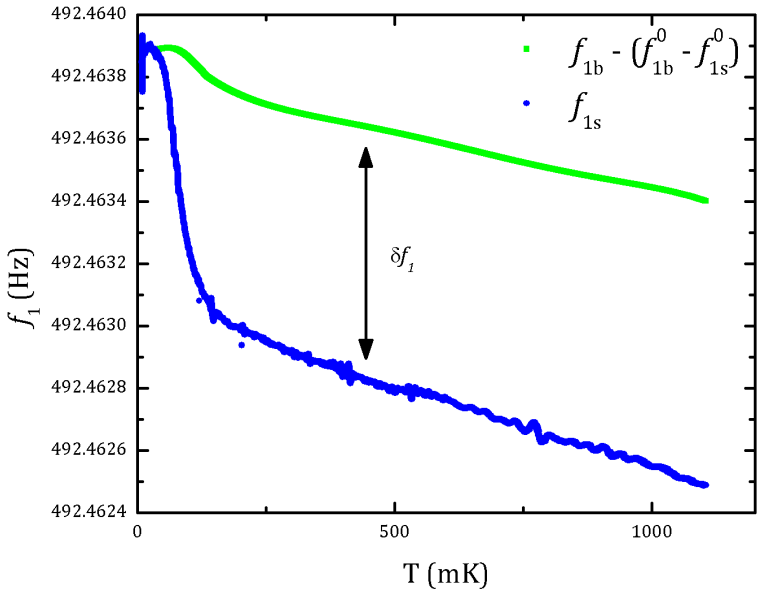

Figure 10, f_1 vs. T for 3ppm solid and the shifted empty cell background: Using the difference between the frequency measured in the solid sample (f_{is}) and the empty cell background (f_{ib}), we can calculate the frequency shift δf_i

Q_i is proportional to the measured amplitude Y_i. The two quantities are simply related by a constant κ_i.

$$Q_i = Y_i * \kappa_i \tag{18}$$

To determine the calibration constant κ_i, Q_i and Y_i are measured via a ring down, at one temperature (usually around 250 mK). The dissipation due to the solid helium sample is the difference between the Q_i^{-1} of the empty cell and the Q_i^{-1} of the cell containing the solid, as seen in Figure 11.

$$\Delta Q_i^{-1} = \frac{Y_{is}^{-1} - Y_{ib}^{-1}}{\kappa_i} \tag{19}$$

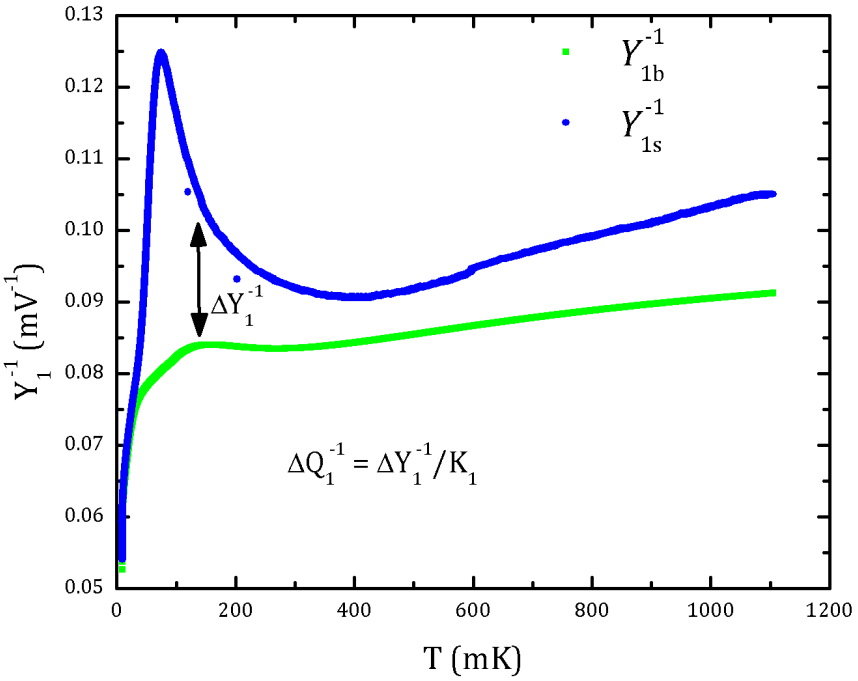

Figure 11, Y_1^{-1} vs. T for 3ppm solid and empty cell: Y_1 is the measured amplitude of TO oscillation the difference in Y_1^{-1} is proportional to ΔQ_1^{-1} the dissipation of the solid sample

1.4 Temperature Dependence Measurements

We made a series of samples at different ^{3}He concentrations (x_3) varying from 0.3 ppm to 25 ppm. [21, 22] Naturally occurring ^{4}He gas typically contains 0.3 ppm ^{3}He. For each of these samples we measured the frequency and amplitude as a function of temperature during a low drive temperature sweep as described in chapter 3 section 5. We then subtracted the background as shown above. Figure 12 and Figure 13 below show the frequency shift and ΔQ^{-1} respectively as a function of temperature for our samples at x_3 = 0.3, 3, 6, 12, and 25 ppm. These allow us to compare the frequency shift and dissipation for both harmonic modes of our oscillator at various concentrations

Our results on frequency shifts are presented in Figure 12 as “reduced frequency shifts” defined for each mode as

$$\frac{\delta f_i(T)}{f_{is}{}^0} = \frac{\left[\left(f_{ib}(T) - \Delta f_i{}^0\right) - f_{is}(T)\right]}{f_{is}{}^0} \qquad (20)$$

$f_{is}{}^0$ is the frequency of loaded TO at our minimum temperature (about 15 mK) depending on x_3. In the zero temperature limit the reduced frequency shift vanishes by definition. It remains, in all samples, at the zero temperature limit below about 40 mK and its magnitude monotonically increases at higher temperatures for both modes. Except in the x_3 = 0.3 ppm sample, the temperature dependence of the reduced frequency shift of the first mode coincides with that of the second mode below about 100 mK. At temperatures greater than 100 mK, changes in reduced frequency of the second mode are greater than those of the first mode. In all samples, except possibly the 0.3 ppm sample, the reduced frequency shifts for both modes continue to decrease as temperature is increased above 200 mK. The lack of data in the 0.3-ppm sample prevents us from making a firm statement about the temperature dependence of the reduced frequency shift above 200 mK in this sample.

The temperature range 50 mK < T < 150 mK, where relatively rapid changes in the reduced frequency shift occurs in Figure 12, has been identified as a signature of the occurrence of NCRI phenomenon. The reduced frequency shifts would become constant if the observed temperature dependence of $f_{is}(T)$ matched that of $f_{ib}(T)$ at temperatures greater than some "onset" temperature, where the fraction of solid sample apparently decoupled from the container or the NCRI fraction (NCRIf) vanishes. Such matching was not found at the low drive levels applied to our TO. Since identifying onset temperatures in our samples is ambiguous, reduced frequency shifts rather than NCRIf are shown in Figure 12. The reduced frequency shift in the 25-ppm sample shows qualitatively distinct

behavior from other samples. In comparison to other samples, there is no temperature range where the reduced frequency shifts vary relatively more rapidly. At temperatures roughly above 150 mK, the frequency shifts decrease linearly (on the logarithmic temperature scale), with the second mode having larger slope than the first. Measured dissipation in the 25 ppm sample is also distinct from other samples (see Figure 13).

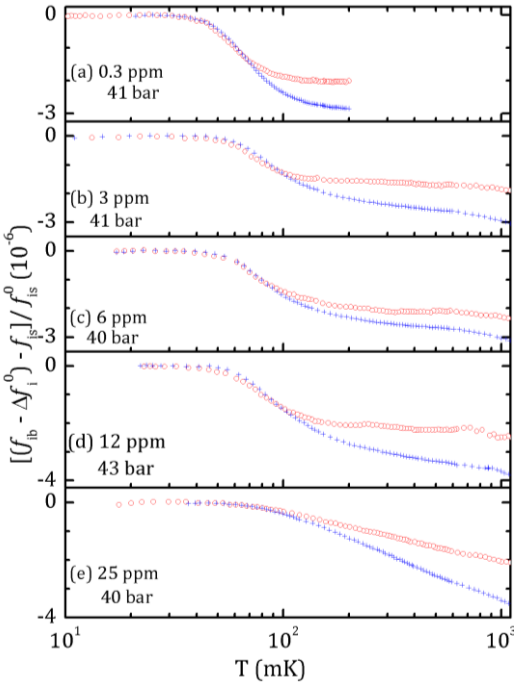

Figure 12, Frequency vs. temperature for several x_3: Temperature dependence of reduced frequency shift of the compound torsional oscillator with annular sample chamber: first mode [(red) open circles] and second mode [(blue) pluses]. Panels (a) ~ (e) show results of solid ^{4}He samples containing ^{3}He impurity concentration of 0.3, 3, 6, 12, and 25 ppm, respectively. Indicated solid pressures are estimated from the loading liquid pressure at 4.2K.

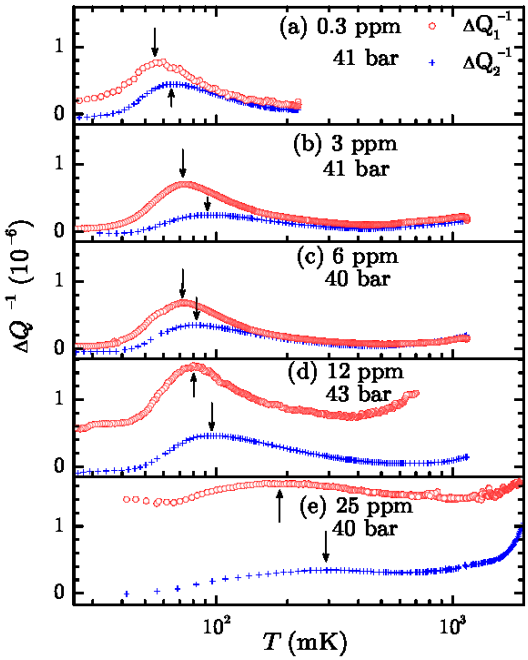

Figure 13, Dissipation vs. temperature for several x_3: Temperature dependence of the change in dissipation from empty to loaded sample chamber: first mode [(red) open circles] and second mode [(blue) pluses]. Measurements are taken simultaneously with those reduced frequency shifts in the samples (with the same panel designations for ^{3}He impurity concentration) as shown in Figure 12. Arrows indicate temperatures where peaks in dissipation occur.

1.5 Dissipation Peak Vs. ^{3}He Impurity Concentration

The arrows in Figure 13 show the temperature (T_{pi}) at which the dissipation peak occurs in each sample for the two modes. The peak temperature in general increases for both modes with increasing x_3. In addition the peaks become broader with increasing x_3. As the peaks move to higher temperatures, the magnitude of the peak dissipation increases as well, with the exception of the peaks in the 25 ppm sample. Additionally, the magnitude of the rise in dissipation above 300-400 mK increases with higher x_3. In the 25 ppm sample, the higher temperature effects in dissipation begin to dominate.

We can compare the T_{pi} we observe to other experiments. To do this we compare the reported [13] T_{50}, the temperature at which 50% of the total frequency shift has

occurred, to our T_{pi}. In Figure 14 we can see that T_{50}^{-1} is close to linear on a log scale of x_3. However, T_{pi}^{-1} deviates from this linear dependence when x_3 is in the range of ~1-15 ppm. In addition T_{pi}^{-1} shows clear frequency dependence: T_{p1}^{-1} is consistently greater than T_{p2}^{-1}. That is, the dissipation peak of the first mode occurs at a lower temperature than that in the second mode. This interesting frequency dependence is analyzed in the next section.

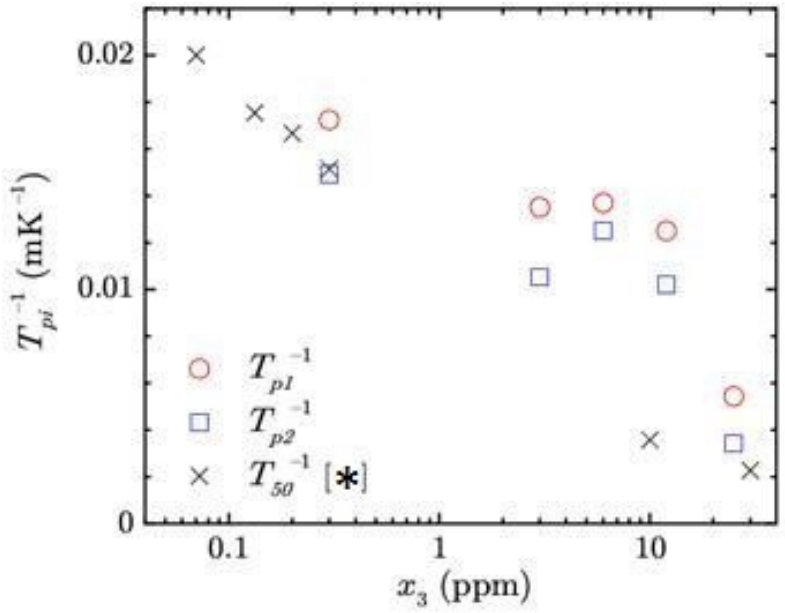

Figure 14, T_{pi}^{-1} vs x_3: First mode [(red) circles] and second mode [(blue) squares]. * "Half-maximum temperatures" or T_{50} (crosses) are taken from Kim et al. [13]

1.6 Fitting Dissipation and Frequency Temperature Dependence

It is generally agreed that dissipation peaks occur at temperatures where an internal dynamical rate τ^{-1} matches the imposed TO frequencies ω_i, or where $\omega_i \tau = 1$. Assuming that the internal dynamics is thermally driven, we consider a simple, activated dynamical time τ given by the Arrhenius form as shown in equation (21).

$$\tau^{-1} = \tau_0^{-1} e^{\frac{-E_0}{k_B T}} \qquad (21)$$

In witch k_B is the Boltzmann constant, τ_0 a characteristic time, and E_0 an activation energy. E_0 and τ_0 are determined from the peak positions as a function of frequency, as seen in Figure 15. This is done by plotting the log of resonant frequency vs T_p^{-1} and fitting with a linear fit. The fits for all measured x_3 have the same slope corresponding to an activation energy E_0/k_B = 430 mK and have ordinate intercepts which are adjusted for best fit for each sample. The intercepts represent the characteristic dynamic rate τ_0.

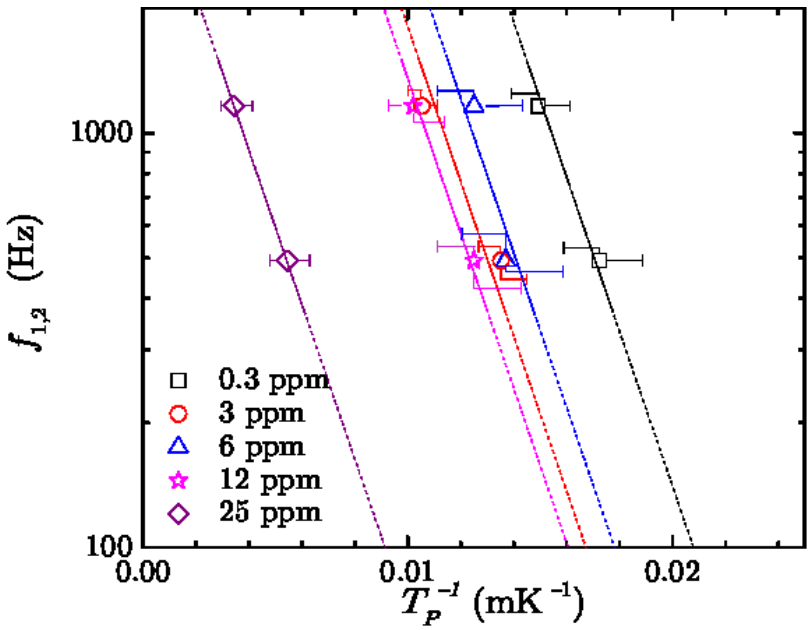

Figure 15, f_i vs. T_{pi}^{-1}: Torsional oscillator frequencies plotted vs. inverse temperature of dissipation peaks, in solid ^{4}He samples with given ^{3}He impurity concentrations. All straight lines have the same slope corresponding to an activation energy E_0/k_B = 430 mK and have ordinate intercepts which are adjusted for best fit for each sample. The intercepts represent the characteristic dynamic rate τ_0

The intercepts of the best fits (shown by a straight line for each x_3 sample in Figure 15) with the set slope specify the values of τ_0 as shown in Figure 16. There is a trend for τ_0 to increase as x_3^{γ}, where $\gamma \sim 2/3$ if $x_3 < 20$ ppm. Both the reduced frequency shifts and dissipation of the 25 ppm sample show qualitatively different behaviors than

the samples with lower ^{3}He impurity concentration. The fitted exponent γ becomes 1∼1.2 if the 25 ppm data point in Figure 16 is included. It appears that τ_0 also changes its dependence on x_3 beyond 20∼25 ppm. It was already noted that the values of T_{50} measured by single-frequency TO techniques by Kim et al. [13] are fairly close to T_{pi} (see Figure 14). Constraining straight lines with the same slope, as shown in Figure 15, by their TO frequencies at T_{50}^{-1} implies values of τ_0 as shown in Figure 16 for their samples. Considering differences in sample chamber geometry, sample growth process, measurement methods, etc., τ_0 extracted from the T_{50} data of Kim et al. [13] overlaps and fits surprisingly well with extrapolation of our results to lower values of x_3. Clearly it is of interest to extend frequency dependence studies like ours to smaller ^{3}He impurity concentrations than we have carried out.

In our observations E_0 appears to be independent of x_3 with a large scatter, and τ_0 increases with increasing x_3. These values of τ_0 as a function of x_3 can be fit by the formula below as shown in Figure 16

$$\tau_0 = \frac{s^2}{g\,v}\, x_3^{\frac{2}{3}}\, e^{\frac{E_0}{T}} \qquad (22)$$

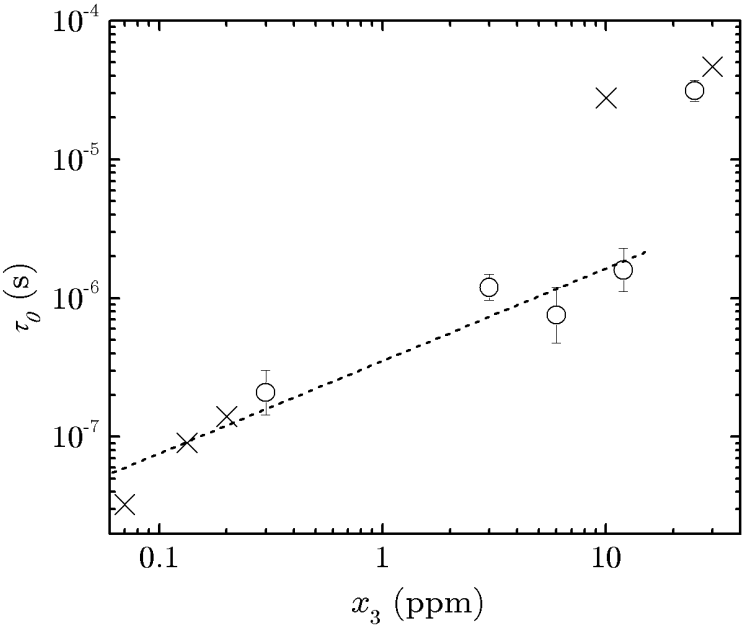

Figure 16, τ_0 vs x_3: Circles are τ_0 from our fits in Figure 15 the dashed line is $\boldsymbol{\tau_0 = 3.5 \times 10^{-7} x_3^{2/3}\ s}$. Crosses are τ_0 calculated from T_{50} data of Kim et al.

It has been suggested by Nussenov et al. [23] that the response of a torsion oscillator can be explained by a generalized rotational susceptibility (χ) without invoking the concept of supersolidity.

$$\chi = \frac{2G}{1 - (i\omega_i \tau)^{\beta}} \tag{23}$$

Where G is a constant (possibly dependent on frequency [24]), ω_i is angular frequency, τ is a relaxation time, and β is an exponent dependent on a particular model. Including the general susceptibility results in extra dissipation and concomitant frequency shifts in the TO response. In our simplified analysis, the "Debye model" response is considered by assuming $\beta = 1$. In this case, the change in dissipation due to sample motion is given by equation (24) below.

$$\Delta Q_i^{-1} = \frac{2\Delta Q_p^{-1}\omega_i\tau}{1+\omega_i^2\tau^2} \quad (24)$$

Here ΔQ_p^{-1} is the magnitude of the dissipation at the top of the dissipation peak equal to G in equation (23).

In Figure 17 we can see the dissipation data fit in two ways. The dotted line is a fit to the data using Equation (22) and Equation (24) above with constant $E = E_0$. The solid curve with broader temperature dependence is fit by allowing a distribution of possible activation energies; a canonical Gaussian N(E) with width w as seen below.

$$N(E) = \frac{1}{\sqrt{2\pi\omega_i^2}} e^{-\frac{1}{2}\left(\frac{E-E_0}{w}\right)^2} \quad (25)$$

The width w in the Gaussian distribution was chosen to fit the first mode data using data normalized to have a peak height of 1. Then the fits were scaled to match the actual peak height in the data. The fits in Figure 17 were determined by setting E_0/k_B=430 mK, the average of the values of E calculated from the peak positions. For each curve, τ was calculated from the midpoint of the line between the mode one and mode two dissipation peaks in the plot of ln(*f*) vs. 1/T as shown in Figure 15.

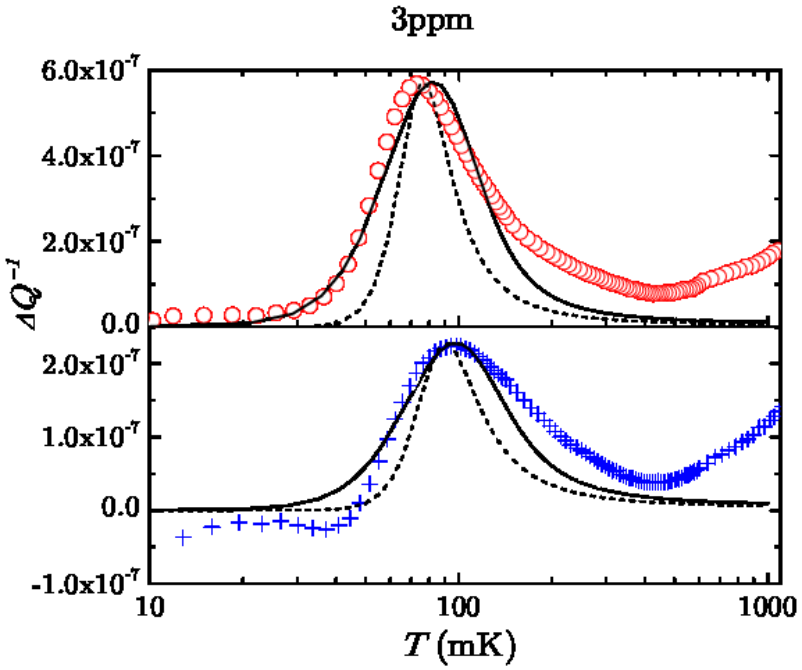

Figure 17, ΔQ^{-1} vs. T with fits: Comparison of dissipation in the x_3 = 3 ppm sample with the dissipation expected from Debye susceptibility. 3ppm dissipation data is shown for mode one [(red) circles] and 2 [(blue) pluses] in panels (a) and (b), respectively. In each panel, curves are dissipation expected (see text) from Eq. (24): assuming single activation energy and $\tau_0 = 1.2 \times 10^{-6}$ s (dashed curves), and allowing Gaussian distribution of activation energy with w/k_B = 120 mK from Eq. (25) (solid curves).

The width w for both modes is determined by the first mode dissipation. If we look at the second mode with several values of w, we find that the second mode is fit by a w within the error on the w determined by the first mode. The values of w as a function of x_3 are shown Figure 18. Widths are determined by fitting temperature dependence of dissipation in each sample using Equations (24) and (25).

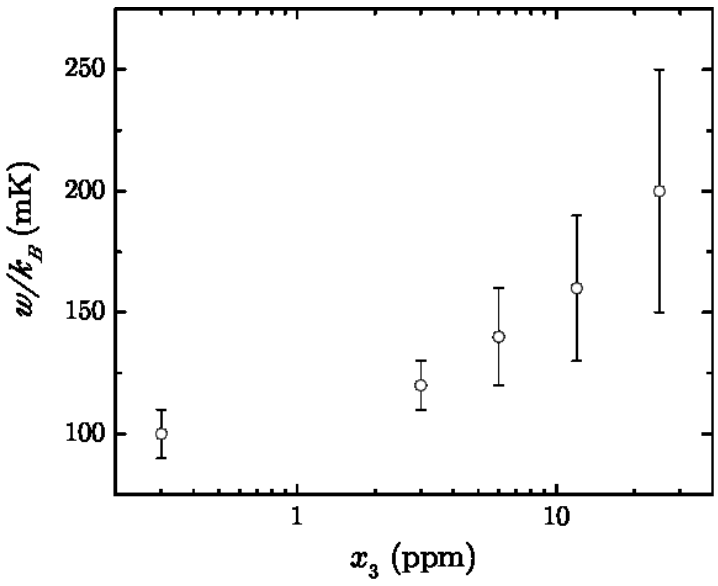

Figure 18, w vs x_3: Width of the distribution of activation energy, as a function of ^{3}He impurity.

1.7 Fitting Frequency Dependence

The frequency curves are determined solely by the fit of the dissipation peak, as seen in Figure 19 using the formula in equation (26).

$$\frac{f_{is} - f_{ib} - \Delta f_i}{f_{is}^0} = \frac{-G}{1 + \omega_i^2 \tau^2} \tag{26}$$

While the first mode fit seems to reproduce data within a factor of two, the second mode fit is always smaller than the first. This is due to the fact that the dissipation peak height of the second mode is consistently lower than that of the first, while the frequency shift normalized by the resonance frequency is larger. This indicates that the model used is not ideal. When the generalized response function above is used to calculate the frequency shift using the parameters generated by fitting the dissipation peak, the magnitude of the frequency shift is too small. The temperature dependence generated by this model, however, fits the observed frequency shift well even though the magnitude is too small.

In fact, the addition of the Gaussian energy distribution in equation (25) used to better fit the dissipation curve improves the temperature dependence of the frequency shift.

In response to the issue of magnitude, we scaled the curves by multiplying the frequency shift by a constant to match the magnitude of the frequency shift as well as its temperature dependence. The scaling factors are 1.7 and 6 for modes one and two respectively. The difference in the frequency dependence of the magnitude of the dissipation peak and the frequency shift is not explained by current models. Future models need to consider that the frequency shift, predicted by using the "Debye model" of the dissipation peak, fits the temperature dependence but not the magnitude. Additionally, these models should consider the fact that with increasing frequency the magnitude of the dissipation peak decreases while that of the frequency shift increases.

The magnitude of the frequency shift normalized to the oscillator frequency increases with increasing frequency, as seen in Figure 19 and Figure 12, but the magnitude of the dissipation peak decreases with increasing frequency, as seen in Figure 17 and Figure 13. These opposed trends mean that a generalized rotational susceptibility as shown above cannot explain the entirety of the frequency shift. Even with a frequency dependent G, the magnitudes of the frequency shift and the dissipation should have the same frequency dependence.

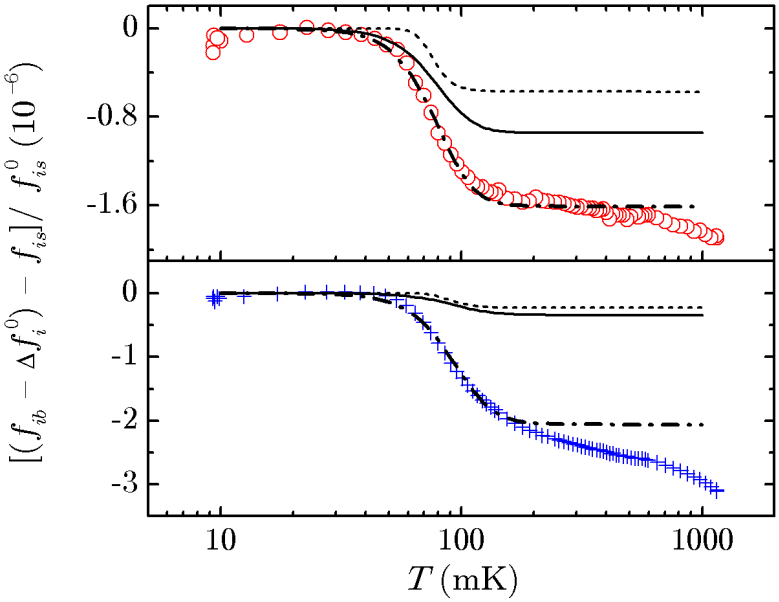

Figure 19, Frequency shift vs T with fits: Comparison of x_3 = 3 ppm sample frequency shift data with those expected from Debye susceptibility using parameters determined from fitting the dissipation data as shown in Figure 17. Dashed and solid curves are those expected from the dissipation shown in Fig. 8 with the single activation energy and with the distribution of activation energy, respectively. Dash-dotted curves are obtained by multiplying the solid curves of the respective modes by constants (see text). Same data (but depopulated for clarity) as shown in Figure 12 are repeated for modes 1 [(red) circles] and 2 [(blue) pluses] in panels (a) and (b), respectively.

These facts indicate that the frequency shift and the dissipation may have a more complex relationship that that of a generalized rotational susceptibility. The larger magnitude of the frequency shift and its different frequency dependence from the dissipation may be due to an additional factor that affects the frequency shift but does not cause additional dissipation.

1.8 Comparison with Other Results on ^{3}He Concentration Dependence

The original work by Kim and Chan showed a large effect on the temperature dependence of the NCRIf due to ^{3}He concentrations of a few ppm. Increasing the concentration of ^{3}He impurities had two effects. First, it caused a broadening of the

period shift, both starting at a higher temperature and changing over a larger range. Secondly, as the ^{3}He concentration became large the period shift reduced in magnitude, vanishing by 0.1% concentration. This suggests that the reason Bishop, Paalanen and Reppy [7] did not see any evidence of supersolidity in their sample was due to its high ^{3}He concentration.

To better understand these effects, Kim et al [13] measured NCRIf on a series of samples of solid ^{4}He with ^{3}He concentrations ranging from 1 ppb to 30 ppm. Samples with concentrations from 1 ppb to 129 ppb were measured by a group at the University of Florida in one torsion oscillator, while samples with concentrations from 70 ppb to 30 ppm were measured at Penn State with a different torsion oscillator. They observed that the maximum value of the NCRIf appears to form a broad peak centered around 1 ppm ^{3}He. In addition, the period shift broadens in temperature, with a higher onset temperature, as ^{3}He concentration is increased. These studies into the effect of ^{3}He concentration (x_3) on NCRIf in solid ^{4}He observed a number of effects beyond the broadening of the temperature dependence of NCRIf. The peak in dissipation that occurs as the frequency shifts also becomes broader with increasing x_3. In addition to the increasing onset temperature, the temperature where the NCRIf is at half its max value (T_{50}) also increases with x_3.

The study by Kim et al [13] fit T_{50} with the following formula based on the idea that $T_{50} = T_{pi}$, the temperature at which dislocations in solid ^{4}He change from being pinned by their own internal network to being pinned by ^{3}He impurities.

$$T_{pi} = -2E_B \left(ln \left[\frac{x_3^2 L_{IP}^3 E_B}{4\mu b^6} \right] \right)^{-1} \quad (27)$$

Where μ = sheer modulus of ^{4}He, b = magnitude of Burger's vector of a dislocation, L_{IB}= average distance between condensed ^{3}He atoms and E_B = Binding energy of ^{3}He atoms to dislocations. This study also found a peak in max NCRIf as a function ^{3}He concentration (x_3), finding that both high and low ^{3}He concentration lead to lower NCRIf values.

1.9 Physical Model For Dependence On ^{3}He Impurity Concentration

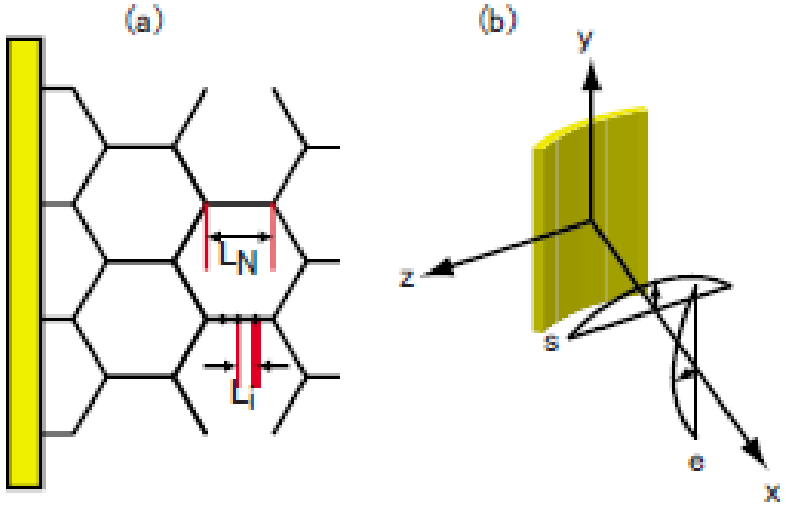

Figure 20, Dislocation structure: (a) Schematic dislocation network in solid helium. L_N: network pinning length, L_i: impurity pinning length. (b) Local coordinate system with two dislocations which glide on yz plane. s: screw dislocation, e: edge dislocation. The small arrows indicate the direction of dislocation motion. Figure from Iwasa [25]

There is a network of dislocations in the sample of solid ^{4}He grown in our experiments. These dislocations are strongly pinned by the network at length L_N and weakly pinned by ^{3}He atoms at length L_i as shown in Figure 20 (a). Ultrasonic studies of ^{4}He have shown that the mobile dislocations are edge dislocations in the Basel plane of the hcp crystal. When the oscillator moves a sheer stress is applied to the dislocations and

they can move as shown in Figure 20 (b); x is the direction from the cylindrical wall to the rotational axis of the TO, y is parallel to the rotational axis and z is the tangential direction of the cylinder. As the TO oscillates, a shear wave propagating in x direction is excited in solid helium which causes displacement in z direction. This movement could lead to the observed frequency shift and dissipation peak.

If the shift in frequency and the peak in dissipation are due to ^{3}He pinning of dislocations, as put forth by Iwasa [25], we can expect $x_3^{2/3}$ dependence for τ_0. This x_3 dependence is due to the diffusion of ^{3}He along the dislocation lines. The diffusion time τ_d of ^{3}He atoms along dislocation lines may be approximated as $\tau_d \approx \frac{s^2}{D}$ where s is some characteristic distance over which ^{3}He moves during a time interval ω_i^{-1}, and $D \approx lv$ is a diffusion constant with mean-free path l and particle velocity v. Suppose that the mean-free path is approximately given by the effective dislocation loop length L. Following Iwasa [25], we write L as a parallel combination of the ^{3}He impurity length L_i and the network pinning length L_N:

$$L^{-1} = L_i^{-1} + L_N^{-1} \tag{28}$$

$$L^{-1} = \left[g x_3^{-\frac{2}{3}} exp\left(-\frac{2W_0}{3T}\right)\right]^{-1} + L_N^{-1} \tag{29}$$

Where $g = 3.4 \times 10^{-7}$ is a constant (as per Iwasa [25]); this leads to the Arrhenius form seen in equation(21).

1.10 Hysteresis

When studying the hysteresis observed in drive dependence measurements at various temperatures, taken as described in chapter 3 section 6, we were unable to obtain empty

cell measurements for every temperature we measured the solid sample at, due to limitations in time. We were still able, however, to make a measurement of the hysteresis effect by measuring the difference in frequency between the initial lowering of dive and the subsequent increase. Using this we can calculate the change in frequency shift suppression $(f_{i\uparrow} - f_{i\downarrow})/f_i$ due to the hysteresis effect as shown in Figure 21. By plotting $(f_{i\uparrow} - f_{i\downarrow})/f_i$ we are able to see how the hysteresis effect changes with temperature. [26]

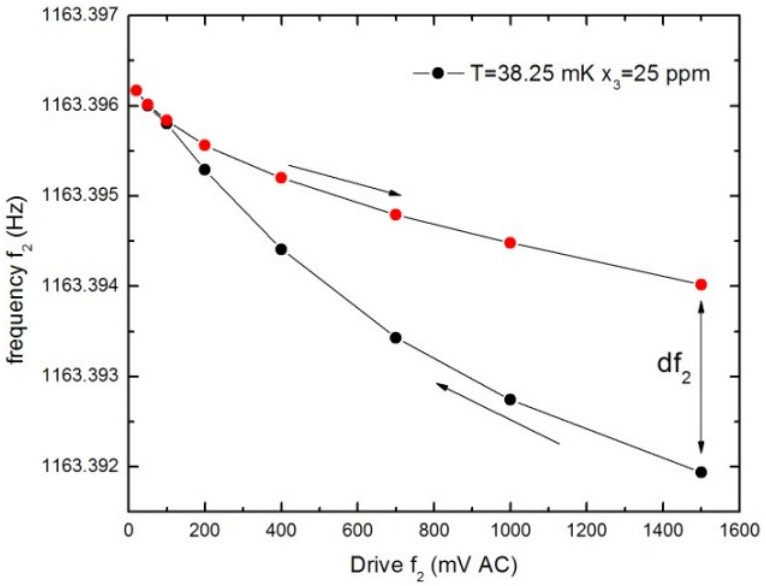

Figure 21, 25 ppm 38.25 mK hysteresis check mode two: The system is cooled at high drive and then the drive is reduced increasing frequency, as shown by the black dots. The red dots show the drive being returned to the initial values in the same series of steps. By looking at the difference between the increasing and decreasing data sets we can measure the size of the hysteresis for comparison.

To determine the temperature where the onset of hysteresis (T_H) occurs we compare plots of hysteresis at several temperatures by looking at the size of the hysteresis at one drive amplitude as a function of temperature as shown in Figure 22. T_H was measured as a function of x_3. Dependence of T_H on x_3 is varied as is shown in Figure 23. In addition, we can compare T_H to T_{pi} from our measurements of dissipation peaks.

Interestingly there does not seem to be a difference in T_H as a function of frequency. Both modes show onset of hysteresis at the same temperature. We can compare T_H to several models as to the mechanism of the hysteresis. First, we can compare with the phase separation curve for the ^{3}He in the sample. The temperature at which ^{3}He condenses on to dislocation lines as a function of x_3 is plotted as a dashed line in Figure 23. Another possible origin is change in sheer modulus due to impurity pinning of dislocations. When impurity pining length matches network pinning length, pinning by ^{3}He atoms begins to effect stiffness. Another thing that was studied was the effect of annealing on hysteresis; we found little effect on T_H after annealing the sample.

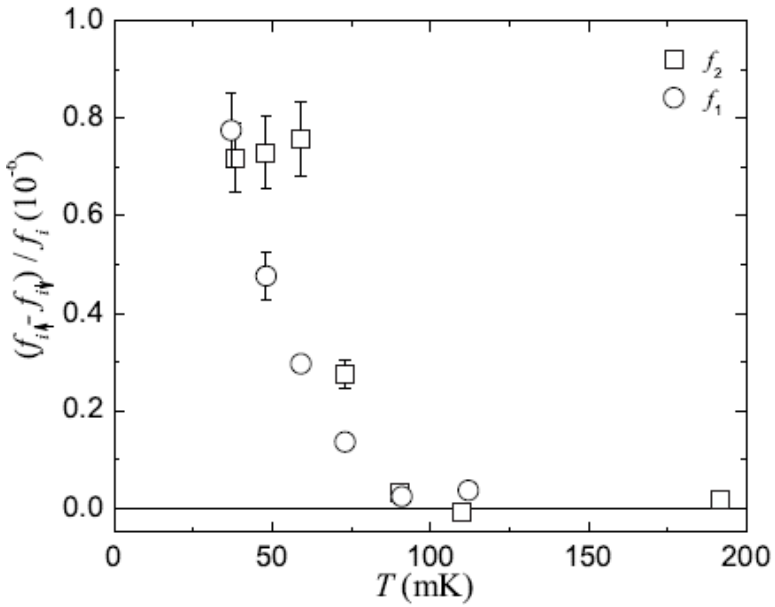

Figure 22, $(f_{i\uparrow} - f_{i\downarrow})/f_i$ vs T at drive of 200 mV for the 25 ppm sample: Hysteretic fractional frequency differences, $(f_{i\uparrow} - f_{i\downarrow})/f_i$ for both mode one (circles) and two (squares). Fractional deviations are evaluated when the drive amplitude is 200 mV in the 25-ppm sample. Fractional deviation vanishes at temperatures higher than a hysteretic onset temperature T_H.

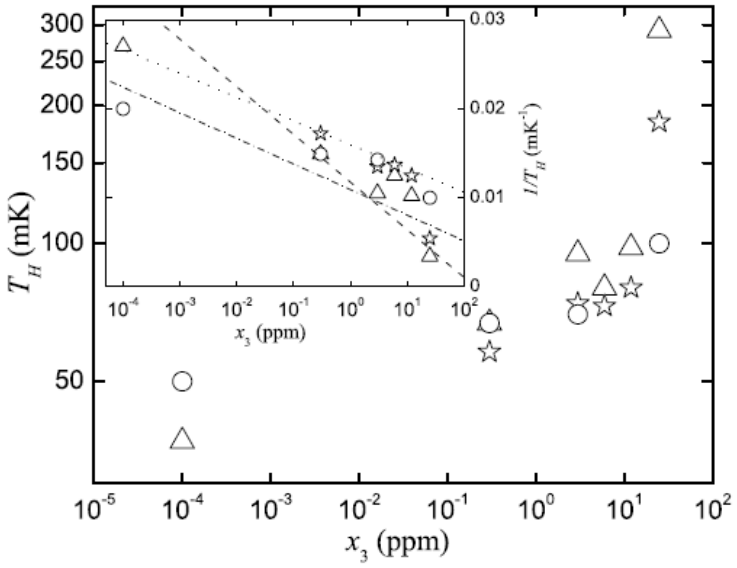

Figure 23, T_H+Tp+phase separation vs x_3: Hysteresis onset temperature (circles) as ^{3}He impurity concentration is varied. Dissipation peak temperatures [13] of the first mode (stars) and the second mode (triangles) are also shown. Uncertainties [13] in peak temperatures, T_{pi} (i = 1, 2), are ±50 mK for the 25-ppm sample and ±5 mK for others. Inset: T^{-1}_H and T^{-1}_{pi} for the same sets of data. Dashed and dash-dotted lines are dislocation pinning length temperature for two different sets of parameters and dotted line is a calculated isotopic phase separation temperature

Within the limited number of samples, we have observed T_H does not depend on mode frequency, drive amplitude, annealing, or refreezing. T_H increases with x_3 and for $x_3 < 20$ ppm is close to the values of T_{pi} particularly considering that T_H has an error of ±10mK due to the nature of our measurements. The observed dependence of T_H on x_3 is close to those of T_{pi} over the whole range of x_3 measured, except possibly $x_3 \geq 20$ ppm, and affirms close link between the dissipation peak and the hysteresis phenomena. The observed hysteresis effects are qualitatively consistent with regarding supersolid phenomena as a vortex matter [27] response but do not exclude other explanations related to dislocation motion. The trend of T_H either decreasing or approaching a constant in the limit of $x_3 \rightarrow 0$ could not be established. If the hysteresis were due to pinning of

dislocations by ^{3}He impurities one would expect T_H to depend on drive level, which it does not.

2: Dependence on Drive Amplitude of Simultaneously Excited Modes.

2.1 Motivation

As the drive amplitude applied to the TO is increased the frequency shift effect is suppressed, approaching the frequency shift seen in the empty cell. In order to study this effect, we cool the system at a high drive and lower the drive amplitude in steps to a low drive where frequency shift is not suppressed. The suppression is measured by looking at the drive dependent frequency shift as a fraction of the low drive temperature dependent frequency shift. Previous work using a compound torsion oscillator (CTO) has shown that the suppression of frequency shift is velocity dependent. [14]

We developed a method of using a CTO to probe both resonant modes simultaneously. To do this we use two function generators with their outputs combined by a summing circuit to drive the system and the signals analyzed through two lock-in amplifiers. If what we are seeing were due to a portion of the helium becoming superfluid, we would expect that both modes would observe the same suppression of frequency shift. Additionally, we would expect this suppression to show velocity dependence as it would be due to the critical velocity effect in the superfluid. This ability to excite and measure both modes simultaneously has allowed us to ask some new questions. If we suppress the frequency shift by increasing the drive amplitude of one resonant mode, would the other mode also show suppression of frequency shift? We set out to answer this and other related questions.

2.2 Procedure

When the drive amplitude is increased the magnitude of the observed frequency shift is reduced, becoming closer to that of the empty cell. This change in frequency shift can be seen as the higher drive levels suppressing the normal low drive frequency shift. To study these phenomena with two modes we first create a state with suppression of the frequency shift due to one mode being driven at high amplitude. To create this state we cool the oscillator while driving one mode (the driving mode) at high amplitude while keeping the other mode (the detecting mode) at sufficiently low amplitude such that suppression does not occur if driven alone. Once the system has been cooled to the target temperature, we can first observe how much suppression occurs in each mode at this high drive. Then to observe the dependence on dive amplitude, we lower the dive amplitude of the driving mode in a series of steps until we reach a low drive amplitude where suppression does not occur if the mode is driven alone. Then the drive amplitude is raised in a series of steps back to its original value in order to observe hysteresis as described in Chapter 3 Section 6.

2.3 Calculating Suppression of Frequency Shift For Drive Dependence

To determine what changes in frequency as the drive is changed are due to the cell itself, the empty cell was measured in a series of procedures using the same driving amplitude sequence and temperatures as the drive dependence measurements with the solid sample.

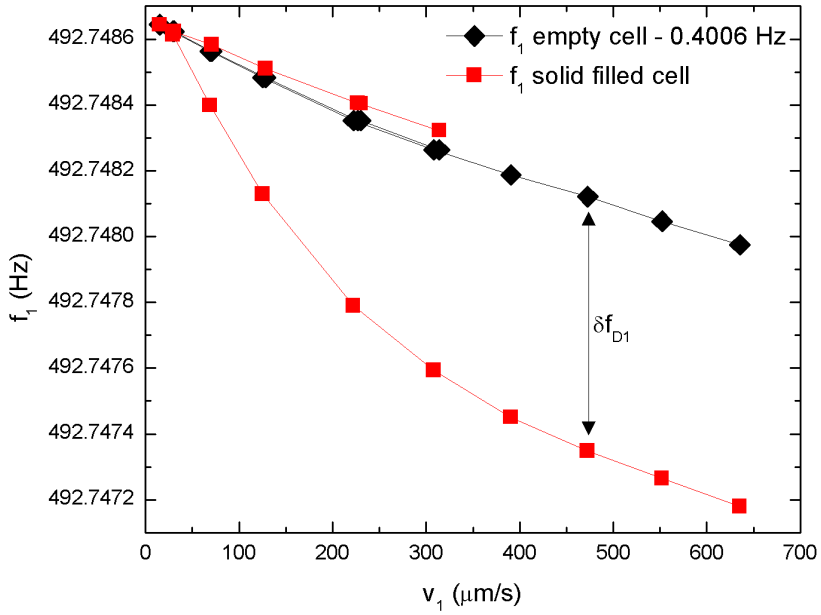

Figure 24, f_2 vs. mode one rim velocity (v_1) and empty cell Background: Using the difference between the frequencies measured in the solid sample and the empty cell background we can calculate δf_{D1} as a function of Rim velocity

We can measure a frequency shift due to drive amplitude (f_{Di}) in a similar manner to the frequency shift seen in Figure 24. The empty cell data is shifted such that the low drive values match. Then the difference between the empty cell data and the sample data is the frequency shift (δf_{Di}) due to the presence of the sample at the drive amplitude.

We want to be able to evaluate the suppression of the frequency shift for both modes. To do so we compare it to an unsuppressed frequency shift due to changes in temperature (δf_{Ti}). The reference we use is the frequency shift at 200mK δf_{Ti}(200mK). 200mK was chosen because it is a temperature where the frequency shift from the zero temperature limit is mostly complete. The resultant suppression is simply δf_{Di} normalized by δf_{Ti}(200mK).

2.4 Results Varying F1 Drive Amplitude

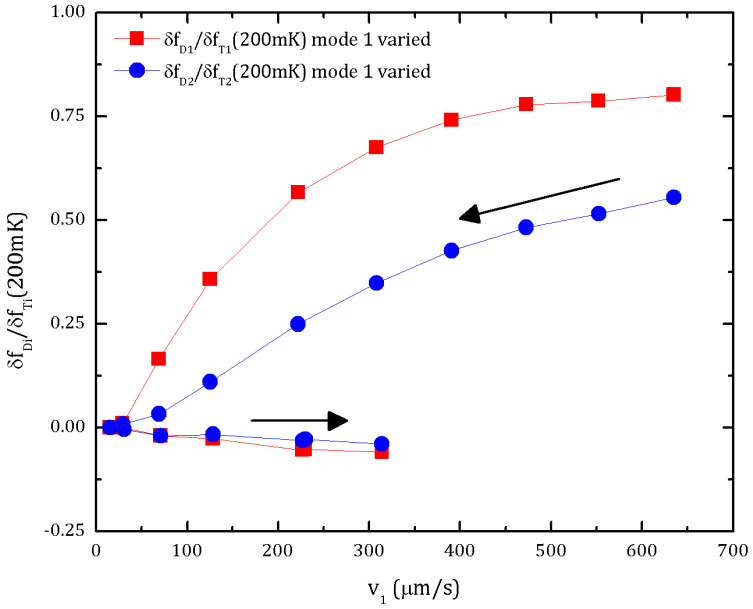

Figure 25, $\delta f_{Di}/\delta f_{Ti}(200mK)$ vs v_1: showing suppression of frequency shift as mode one drive amplitude is varied. Arrows indicate direction of drive level change showing the hysteresis as described in section 1.10 of this chapter on page 43.

Figure 25 shows the results when the drive amplitude of mode one is varied. We observe a frequency shift in mode one consistent with a $\delta f_{D1}/\delta f_{T1}(200mK)$= 80% suppression of frequency shift at a rim velocity of ~650 μm/s. However, mode two shows only $\delta f_{D2}/\delta f_{T2}(200mK)$ = 56%. The shift observed by mode two is equivalent to ~2/3 of the suppression of mode one. As the drive amplitude is varied no sudden changes in suppression are observed for either mode. Were the frequency shift due to superfluidity one would expect that the critical velocity effect to suppress the frequency shift of both modes equally.

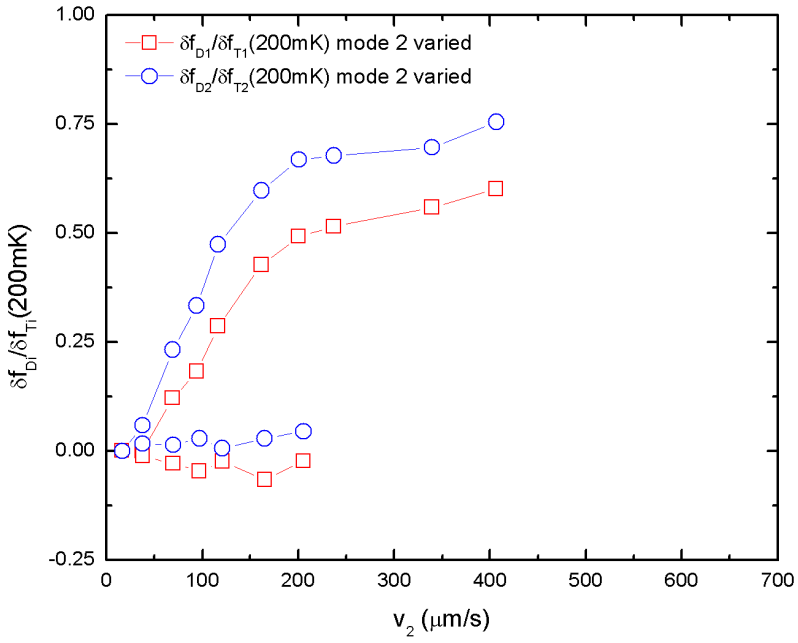

Figure 26, $\delta f_{Di}/\delta f_{Ti}(200mK)$ vs v_2: Shows suppression of frequency shift as mode two drive amplitude is varied

Figure 26 shows when the drive amplitude of mode two is varied the frequency shift observed in both mode one and mode two shows similar amounts of suppression with $\delta f_{D1}/\delta f_{T1}(200mK)=75\%$ and $\delta f_{D2}/\delta f_{T2}(200mK)=60\%$ at the high dive level.

2.5 Comparison Of All Permutations Of Driving And Detecting Modes

To compare the shift in frequency due to increase in drive amplitude to the shift in frequency due to increase in temperature, we look at the frequency shift normalized by the frequency shift at 200mK a temperature at which the shift in frequency due to temperature is complete in 0.3 ppm ^{3}He. This normalized frequency shift can be noted as $\delta f_{Di}/\delta f_{Ti}(200mK)$; this allows us to compare the two modes by looking at $\delta f_{Di}/\delta f_{Ti}(200mK)$ as a suppression of the shift due to cooling. One thing we can observe about the frequency shift due to increased drive is that the change in both modes is linear as a function of $\log(v_i)$, as seen in Figure 27.

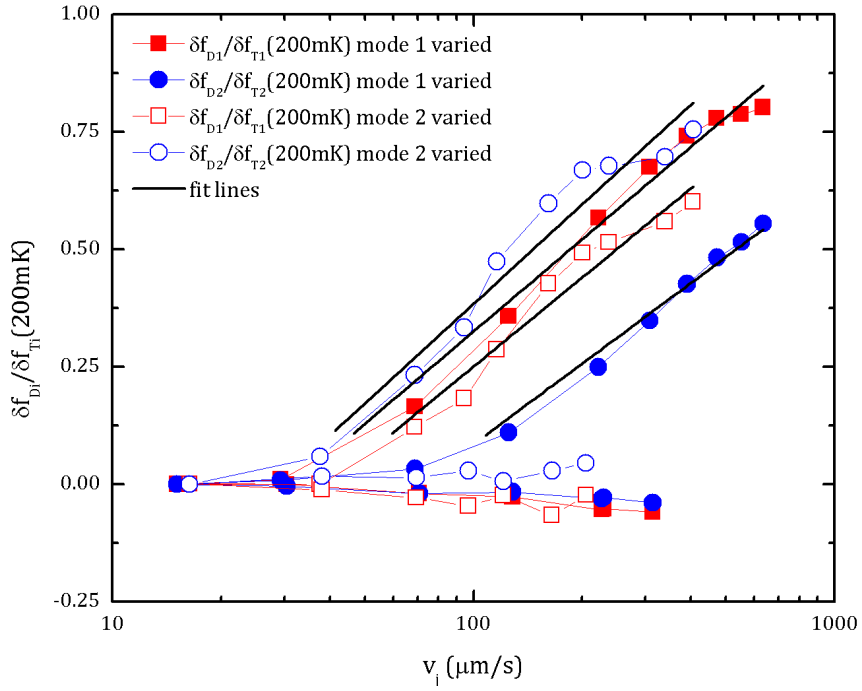

Figure 27, $\delta f_{Di}/\delta f_{Ti}(200mK)$ vs. $\log(v_i)$ with linear fits: Slopes (-0.27365, -0.24744, -0.28332, -0.30578) for ($\delta f_{D1}/\delta f_{T1}(200mK)$ vs $\log v_1$, $\delta f_{D2}/\delta f_{T2}(200mK)$ vs $\log v_1$, $\delta f_{D1}/\delta f_{T1}(200mK)$ vs $\log v_2$, $\delta f_{D2}/\delta f_{T2}(200mK)$ vs $\log v_2$) respectively

When this data is fit linearly, we find that the slopes of $\delta f_{Di}/\delta f_{Ti}(200mK)$ vs $\log(v_i)$ are the same for all the runs at each temperature. This implies that the suppression may be due to the same mechanism in all of the cases. The origin of the horizontal shift of the curves for different modes is not clear. While three of the curves are clustered closely together, the suppression of mode two as the detecting mode when mode one is the driving mode is a clear outlier. Mode two as the detecting mode shows a significantly larger intercept in $\log(v_i)$. One possible origin of this horizontal shift may be an asymmetry between how higher frequency modes affect lower frequency modes and how lower frequency modes affect higher frequency modes. Another possible origin is a difference in how the detecting modes are affected by drive level as opposed the driving modes.

2.5.1 Comparing driving mode suppressions

It is interesting to see if the frequency shifts depend on rim velocity, displacement, or acceleration. The suppressions of mode one and mode two, as a percentage of maximum frequency shift, collapse upon one another as a function of rim velocity of the driving mode, as seen in Figure 28. The suppressions do not match each other if they are plotted against the rim displacement or acceleration (a_i). This collapse occurs at all three temperatures (10 mK, 25 mK and 60 mK) where data was taken. It occurs both when hysteresis is observed and above the temperature when hysteresis stops. In addition, this collapse has also been previously observed when only one mode is driven [14].

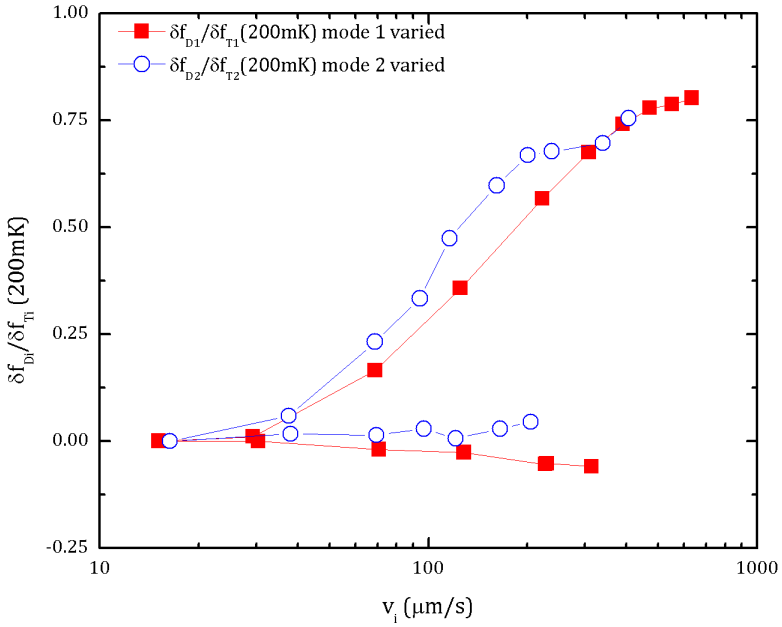

Figure 28, $\delta f_{Di}/\delta f_{Ti}$(200mK) vs v_i: Showing the suppression effect of increased drive on the driving mode at 10 mK.

2.5.2 Comparison of detecting mode suppressions.

When comparing the suppression of the detecting mode in each case the curves do not collapse as a function of the rim velocity of the driven mode, as seen in Figure 29. The

suppression in both cases does collapse as function of the rim acceleration of the driving mode, as seen in Figure 30. This collapse occurs at all of the temperatures measured: 10 mK, 25 mK and 60 mK.

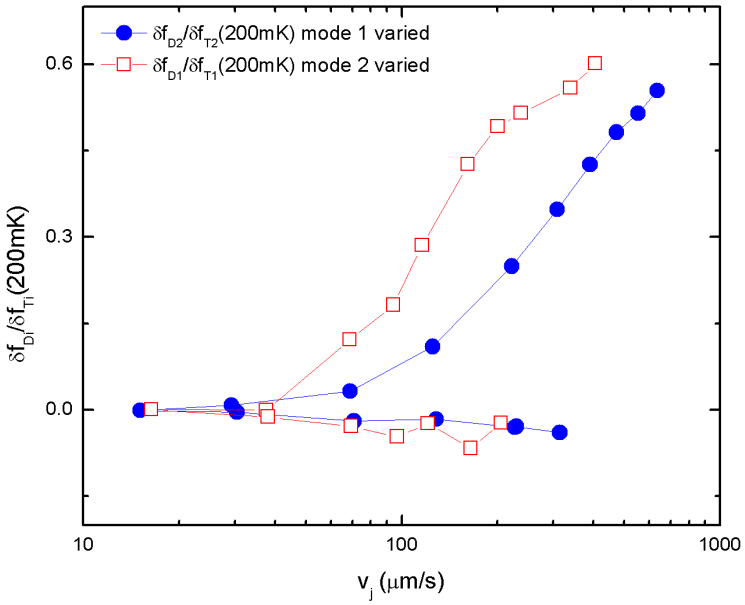

Figure 29, $\delta f_{Di}/\delta f_{Ti}(200mK)$ vs v_j $i \neq j$: Showing the suppression effect of increased drive on the detecting mode at 10 mK.

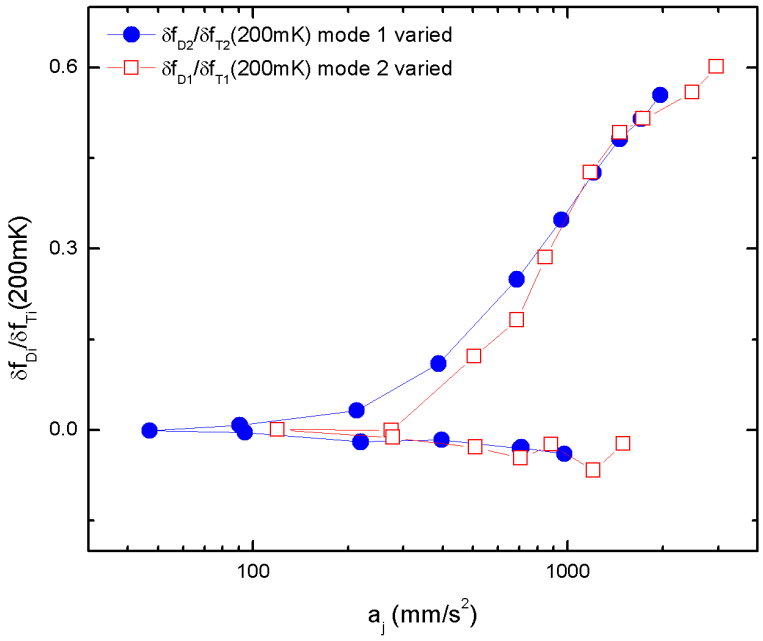

Figure 30, $\delta f_{Di}/\delta f_{Ti}(200mK)$ vs a_j $i \neq j$: Showing the suppression effect of increased drive on the detecting mode at 10 mK indicating a possible acceleration dependence.

2.6 Interpretation

One of the things that we see is that the drive dependence of the frequency shift is linear as a function of $\log(v_i)$. This is predicted by Anderson's [27] model of ^{4}He as a vortex fluid. If the frequency shift was due to supersolidity we would expect a sharp step similar to what is seen in superfluid liquid ^{4}He. All of the measurements at both frequencies at the same temperature have the same slope. This indicates that the slope is independent of frequency and is only a function of temperature. In addition, driven mode suppression collapses as a function of rim velocity. This indicates that, the mechanism behind the frequency shift of a mode is dependent on the velocity of the mode itself. Detecting mode suppression collapses, however, as a function of rim acceleration. This indicates that the mechanism by which the modes affect each other may be acceleration dependent, such as shear stress. But this apparent acceleration dependence could be an artifact of the specific

two frequencies we used. Especially as, when the driven mode is mode two, the suppression of mode one and mode two are close to collapsing on each other as a function of rim velocity, at both 10 mK and 60 mK, as seen in Figure 26. There is no similar collapse when mode one is the driven mode, as seen in Figure 25. This indicates the possibility that mode two affects mode one completely as it is a higher frequency, but mode one at a lower frequency has a reduced effect on mode two.

All the frequency shift data can be well represented by logarithmic functions of the rim velocity, as seen in Figure 27. (The rim acceleration is the rim velocity multiplied by the frequency, so the data is also well represented by logarithmic functions of rim acceleration). Additionally, all of the slopes are the same within 5%. This connection between the slopes implies that both the effect on the detecting modes and the effect on the driving modes are caused by the same mechanism. The suppressions of mode one as mode one is varied, mode one as mode two is varied and mode two as mode two is varied collapse on each other as a function of rim velocity. These facts reinforce the idea that higher frequency modes affect all lower frequencies (unpinning shorter dislocations unpins all longer ones) but lower frequency modes do not affect all that higher frequency modes see (longer dislocations being excited cannot unpin the shorter ones.)

If the system was described by a simple superfluid model, where a portion of the solid helium sample decouples from the oscillator by becoming a superfluid, we would expect that the suppression of both the detection and driving mode would be the same. Also such suppression would be expected to be velocity dependent. Our observations, however, show that when mode one is the driving mode the suppression of the detection mode is ~2/3 that of the driving mode. Also, the suppression of the detection mode

appears to show rim acceleration dependence, not rim velocity dependence. Therefore, the observations do not support a simple superfluid model.

In the simple superfluid model, the origin of the observed frequency shift is a portion of the solid decoupling from the oscillator by becoming a superfluid. Such decoupling would be observed identically at all frequencies. The observed drive dependence is due to less solid decoupling at higher velocities. Once again this effect would be frequency independent. If one looks at the decupled fraction or NCRIf, the difference between modes one and two is more than a factor of two. This is illustrated in Figure 31.

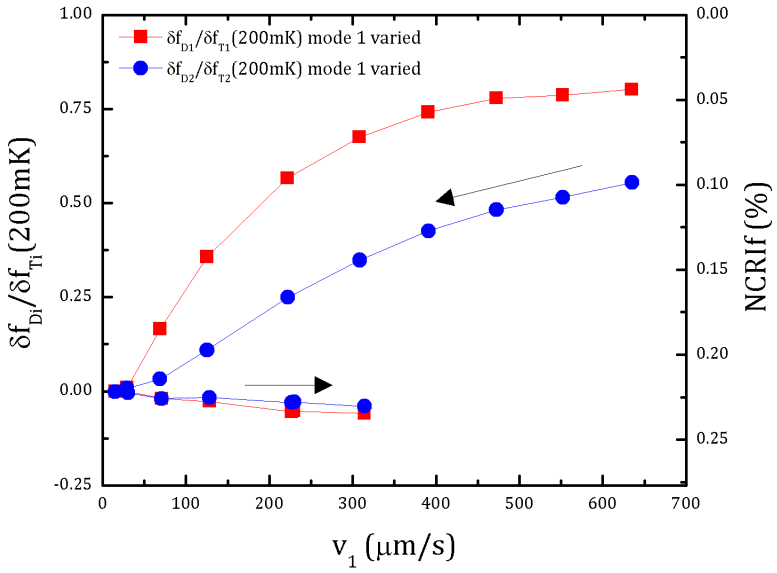

Figure 31, $\delta f_{Di}/\delta f_{Ti}(200mK)$ and NCRIf vs v_1: This is a copy of Figure 25 with the addition of a scale showing a calculated NCRIf based on the assumptions of the simple superfluid model.

2.6.1 Models compared to effects

The most basic model for the origin of the TO effects proposed is that a portion of the solid becomes a superfluid and decouples from the oscillator. This superfluid component

would recouple with the oscillator when the magnitude of the velocity of the oscillator is higher that some critical velocity. As the amplitude of the oscillation increases, the oscillator spends a larger fraction of time at velocities greater than the critical velocity. The fraction of time spent above the critical velocity can be used to predict the observed suppression of frequency shift. This model predicts suppression of the form shown in equation (30) where v_{crit} is the critical velocity and v is the rim velocity.

$$\frac{\delta f_D}{\delta f_T(200mK)} = \frac{2}{\pi}\, cos^{-1}\left(\frac{v_{crit}}{v}\right) \qquad (30)$$

This simple superfluid model would predict a sharp onset as the critical velocity is reached followed by a rapid saturation of suppression. The prediction is inconsistent with the linear in $\log(v_i)$ dependence observed, as displayed in Figure 27. Were the effect a simple superfluid one would expect that all suppression observed would be velocity dependent, which is inconsistent with the observed acceleration dependence in cross drive measurements. Additionally, the fact that when mode one is increased, mode two measured less suppression than mode one is not expected as, if this were a simple superfluid, the decoupling measured by both modes would be the same.

Thus, the simple superfluid model is inconsistent with almost all of our observations. Other models do explain some of the observed phenomena but not all. The vortex liquid model proposed by Anderson [27] predicts amplitude dependence that is linear in $\log(v_i)$ as we have seen. Both the dislocation movement and superglass models describe a distribution of objects with a critical frequency. In both cases, this distribution is what determines the amplitude dependence. So an appropriate distribution can lead to the observed linear in $\log(v_i)$ dependence. In the dislocation movement these are the

pinned dislocations which have a natural resonant frequency. In the superglass model these are the various glassy pockets which have a critical frequency above which they liquefy. In both cases higher frequency modes affect lower frequency modes but not the other way around. Glassy pockets liquefy if the frequency is above a critical frequency, and the unpinning of shorter higher frequency dislocations cascades to unpin longer dislocations but not the other way around.

2.6.2 Dislocation movement

It has been proposed that the frequency shift seen in ^{4}He samples is due to the pinning of dislocations by ^{3}He impurities [25]. This pinning increases as temperature decreases. The increased drive amplitude also increases dislocation movement and makes pinning more difficult. Each mode sees a different set of dislocations so when one mode is excited the effects on the others are non-identical. The range of dislocation sizes excited by the driving signal is a function of frequency. Prevention of the pinning by ^{3}He impurities due to increased movement of one set of dislocations could allow the excitation of one mode to effect the other. While different sets of dislocations are excited by different frequencies, there is overlap between these sets. Thus the increase in unpinned dislocations due to the high drive amplitude of the driving mode could lead to the suppressed frequency shift observed by the detecting mode. The acceleration dependence may indicate how the dislocations at different frequencies affect each other via the prevention of pinning.

When mode two is excited both modes have about the same suppression. But when mode one is excited mode two has ~2/3 the suppression, as seen in Figure 27. The

model proposed by Iwasa [25] explains the suppression of the frequency shift with increased amplitude by proposing that the increased movement of dislocations unpins them. The force on a dislocation segment of length L_N is $F = L_N b\sigma$ where σ is the sheer stress on the dislocation and b is the Burgers vector. The magnitude of this force is proportional to the length of the dislocation segment, so a force that unpins shorter dislocations also unpins all longer dislocations. Thus the excitation of short dislocations via higher frequency oscillations should affect longer dislocations observed by lower frequency modes, but the reverse is not necessarily the case. This corresponds with what we see using the CTO where the higher frequency mode's movement has the same effect on both modes white the lower frequency mode has a reduced effect on the higher one.

2.6.3 Shear modulus

Day and Beamish [28] directly measured the shear modulus of solid ^{4}He and they found an anomaly in temperature dependence of the sheer modulus. As the solid ^{4}He sample is cooled, its shear modulus increases. This increase has a temperature dependence that is very similar to that seen in the frequency shifts seen in TO experiments. In addition, this anomaly in shear modulus shows many of the same qualitative features as the frequency shift such, as its ^{3}He dependence. The cause of the frequency shift we observe cannot be only due to the sheer modulus shift as the observed effect is too large. Finite element analysis of single mode oscillators was used to generate estimates of the sheer modulus change required to create the observed frequency shift [29]. These estimates generate values between 2 and 5 times as large as the observed change in sheer modulus. This indicates that the sheer modulus shift alone cannot be the origin of the observed

frequency shifts. In addition, the sheer modulus effect has an amplitude dependence similar to that of frequency shift. The sheer modulus effect is a stress strain effect which would be acceleration dependent. There is the possibility that the observed acceleration dependence in the detecting mode situation is due to the fact that suppression between the two modes is mediated by the change in sheer modulus.

2.6.4 Questions for further study

We have only studied this phenomenon at the two frequencies of our current CTO. It would be interesting to see if the results are consistent at other frequencies. It would also be interesting to see what happens to suppression if the detecting mode was held at a drive amplitude large enough to cause suppression. How would suppression for two sources combine?

Chapter 5: Summery

1: State of Affairs Before This Work

In 1969 Andreev and Liftshits [1] proposed that motion of vacancies in solid helium could allow for superflow in a solid or supersolidity. In 2004 evidence for supersolidity was reported in experiments of torsional oscillator (TO) containing solid ^{4}He in vycore glass as well as in bulk ^{4}He. The evidence was an increase in resonance frequency of the TO indicating a decrease in moment of inertia; this is consistent with superflow causing decoupling of part of the solid.

2: Objectives and Questions

Given the above fairly convincing, if controversial proposal, our goal was to use our compound oscillator to further investigate the supposed supersolid properties. We asked two questions. First, how does ^{3}He impurity level (x_3) affect the observed frequency shift and dissipation peak? How does the ^{3}He impurity effect depend on the frequency of the TO? Second, how can we investigate the critical velocity effects using the compound oscillator which is capable of probing the sample response at two frequencies simultaneously?

3: Observations

3.1 ^{3}He Dependence

The dissipation peak occurs at temperature T_{pi} which depends on x_3 as $x_3^{2/3}$. This dependence suggests that diffusion of ^{3}He along dislocation lines is responsible for dissipation peak position. This also suggests that the dissipation peak and its

corresponding frequency shift may be due to dislocation movement affected by pinning due to ^{3}He impurities.

The dissipation peaks can be fit using a Debye rotational susceptibility model and a Gaussian distribution of activation energies, as explained in Chapter 4 Section 1.6. On the other hand, the observed frequency shift is not fully explainable by this Debye model. This excess frequency shift can be fit by multiplying the Debye model curve by a constant for each TO mode. The shape of the temperature dependence is the same but the magnitude of the shift is larger than predicted by the model. In addition, the scaling constants are similar for multiple ^{3}He concentrations at the same frequency. This implies that the frequency shift may consist of two components that are interdependent such that the phenomenon responsible for the dissipation peak is affecting a second mechanism that does not appear in the dissipation data.

3.1.1 Effect of ^{4}He in torsion rod

One of the suggested origins of the effect observed is the solid ^{4}He in the fill line in the center of the Torsion rod of the oscillator. As the sheer modulus increases with decreasing temperature this would change the torsional spring constant of the rod. We were able to examine the possible effects that solid ^{4}He within the fill line in three independent TOs fabricated with different sample chambers. All of these chambers were attached to an identical torsion rod system. The measured mode frequencies, loading frequencies, frequency shifts at low temperatures, and estimated frequency shifts expected from the changes in shear modulus of solid ^{4}He contained within the torsion rod are all tabulated for the three sample chambers in Table 1. The observed maximum

increase in shear modulus [28] of solid ^{4}He samples grown by blocked capillary method is near 30%. The expected shift in the ith mode frequency ($\delta f_{i\mu}$) from this change in shear modulus of solid ^{4}He within the torsion rod (assuming the two rods in our double compound TO are identical) is estimated by equation (31).

$$\delta f_{i\mu} = 0.3\left(\frac{1}{2}\right) f_i \left(\frac{\mu_4}{\mu_{BeCu}}\right)\left(\frac{r_4}{r_{BeCu}}\right)^4 \qquad (31)$$

Where $\mu_4 \sim 1.8 \times 10^8$ is the shear modulus of solid ^{4}He, $\mu_{BeCu} = 5.8 \times 10^{11}$ the shear modulus of the BeCu rod, r_4 the radius of fill tube and r_{BeCu} the radius of the BeCu rod (numerical values given in cgs units). As can be seen in Table 1 below, the measured δf_i in the cylindrical sample chamber is indeed quite close to $\delta f_{i\mu}$. Note, however, that the ratio $\delta f_2/\delta f_1$ is significantly larger than $\delta f_{2\mu}/\delta f_{1\mu}$ (= f_2/f_1). The measured frequency dependence of δf_i does not match that of the shear modulus effect. In the annular sample chambers, the measured δf_i is larger than the calculated $\delta f_{i\mu}$ by a factor between 1.5 and 6 depending on the mode. Furthermore, the frequency dependence of the shift as indicated by the ratio $\delta f_2/\delta f_1$ is much greater than that of the ratio $\delta f_{2\mu}/\delta f_{1\mu}$ calculated from the maximum 30 % expected change in shear modulus. From these clear discrepancies between δf_i and $\delta f_{i\mu}$, one can conclude that the major portions of observed frequency shifts, as well as response amplitudes, in our TO result from the interaction between the solid ^{4}He sample and its chamber, not the torsion rod. The ratio $\delta f_i/\Delta f_i$ represents the NCRI fraction, as it has been called in the literature. If this fraction is to be interpreted as superfluid fraction, it is expected to be independent of frequency. Table 1 shows that $\delta f_i/\Delta f_i$ is independent of the mode frequency in the cylindrical chamber, but it becomes increasingly more dependent on frequency in thinner annular channels. Barring extremely

strong size dependence on restricted geometry, this frequency dependence is contrary to interpreting the frequency shift as due only to a superfluid fraction. The observed dependence on the width of the annular chamber is not in proportion to the square of the annulus width, as predicted by considering the elastic influence of solid ^{4}He on TO.

Sample chamber	cylinder			1 mm wide annulus			0.2 mm wide annulus		
	i=1	i=2	ratio	i=1	i=2	ratio	i=1	i=2	ratio
f_i(Hz)	497	1171	2.4	493	1164	2.4	465	1092	2.3
Δf_i(Hz)	0.667	2.05	3.07	0.4	1.2	3	0.173	0.313	1.8
δf_i(mHz)	0.67	2.05	3.06	0.995	3.36	3.4	1.2	8.1	6.8
$\delta f_i/\Delta f_i$	0.001	0.001	1	0.0025	0.0028	1.1	0.0069	0.026	3.7
$\delta f_{i\mu}$(mHz)	0.62	1.47	2.36	0.62	1.46	2.36	0.58	1.37	2.35

Table 1: Effects of sample shape on frequency

3.1.2 Hysteresis

When the TO drive amplitude is decreased and then increased back up, the observed frequency shift and dissipation are not reversible. This hysteresis occurs only at temperatures below an onset temperature T_H. The observed dependence of T_H on x_3 is similar to that of T_{pi}; this similarity of dependence on x_3 shows a link between the onset of hysteresis and the dissipation peak. Unlike T_{pi}, T_H does not depend on mode frequency, annealing, refreezing or drive amplitude. However, T_H does depend on x_3. The fact that T_H depends on x_3 but not on the other factors above indicates that the hysteresis effect involves a property of the ^{3}He diffused throughout the ^{4}He solid. As a function of x_3, T_H is similar to ^{3}He phase separation temperature below which ^{3}He condenses on to dislocation lines. The observed hysteresis effects qualitatively are consistent with regarding the observed phenomena as a vortex matter response [27] but do not exclude other explanations based on dislocation movement.

3.2 Drive Dependence

Looking at each frequency alone shows velocity dependence as would be expected by a phenomenon due to superflow limited by critical velocity effects. On the other hand, the onset of critical velocity effects is smooth and continuous; lacking the sharp onset seen in other superfluid systems such as liquid ^{4}He. The frequency shift due to increased drive amplitude is linear in $\log(v_i)$. Such a dependence on $\log(v_i)$ is consistent with the vortex fluid model [27]. Such effects could also be caused by dislocation movement or superglass.

The drive dependences are all linear in $\log(v_i)$ with all measurements, at the same temperature, having the same slope. Looking at the measurements of the non-driving mode we found that the slope as function of $\log(v_i)$ was same for all runs at each T, independent of whether the mode was varied or fixed. In addition the detecting modes showed what appeared to be acceleration dependence. This acceleration dependence indicates a possible connection to the sheer modulus changes as sheer stress is a function of acceleration. When mode one is the driving mode, mode two has approximately 2/3 the suppression of mode one. When mode two is the driven mode, mode one shows similar suppression to mode two.

The frequency dependence of suppression is inconsistent with the simple super fluid model. In this model the suppression is simply a function of the amount of helium that has stopped being superfluid, so suppression would be frequency independent. The fact that mode two has a larger effect on mode one that mode one has on mode two is consistent with the dislocation movement model. This model predicts that higher frequencies would have a larger effect on lower frequencies than lower frequencies

would have on higher. In the dislocation movement model, the unpinning of dislocations cascades to the network pinning length. This means the unpinning shorter dislocations with a higher resonate frequency unpins longer ones but not the other way around. So higher frequencies will affect what lower frequencies see but lower frequencies will not affect all that higher frequencies see. A similar effect is seen in the superglass model. Neither of these models, however, predict an acceleration dependence or that the measurements will be linear in $\log(v_i)$. Overall, no model yet provides a complete discretion of these phenomena.

3.3 Connections to Other Recent Work

Since we preformed our experiments, Chan redid the study of ^{4}He in Vycor. This was to correct for the disk of bulk ^{4}He in their oscillator during the first test. [30] They built a new oscillator that eliminated any open space for bulk helium. Once all of the bulk helium was eliminated, no frequency shift from the sample was observed. This means that the effects we are observing in bulk ^{4}He do not appear in the vycor. Were the sample a supersolid, the vycor would show a frequency shift due to the onset of super flow. The vycor effectively pins all movement of dislocation structures which are on the scale of a few microns, so the pore diameter of 7nm prevents the formation of the structures seen in bulk helium. The conclusion that superflow is not the cause of the effects observed in ^{4}He is consistent with our results, which are more consistent with dislocation pining.

4: Conclusions

Much of what we observed was inconsistent with solid ^{4}He being a superfluid similar to other known superfluids such as liquid ^{4}He. The frequency dependent effects and x_3

dependence observed are not described by a simple superfluid model. The drive dependence and hysteresis were both too gradual for a simple superfluid. Additionally when mode one was excited, mode two had only 2/3 the suppression this is inconsistent with a basic superfluid model where the suppression would be the same for both modes. More complex models, however, do explain several of the observed phenomena. The $\log(v_i)$ slope in the amplitude dependence is described by the vortex liquid model proposed by Anderson [27].

The observed ^{3}He dependence could be explained by dislocation movement and ^{3}He pinning. Additionally, the asymmetry of the cross mode drive dependence where if mode one is excited mode two has less suppression, but if mode two is excited mode one has the same suppression could be explained by both the dislocation movement and superglass models. In the dislocation movement model, the unpinning of dislocations cascades to the network pinning length. This means the unpinning shorter dislocations with a higher resonate frequency unpins longer ones but not the other way around. So higher frequencies will affect what lower frequencies see but lower frequencies will not affect all that higher frequencies see. The same sort of system exists in the superglass model where pockets of glassy material have a critical frequency above which they liquefy leading to the same sort of behavior.

Bibliography

[1] A. F. Andreev and I. M. Lifshitz, "Quantum theory of defects in crystals," *Sov. Phys.—JETP 29,* p. 1107, 1969.

[2] G. V. Chester, "Speculations on Bose-Einstein Condensation and Quantum Crystals," *Physical Revew A,* vol. 2, pp. 256-258, 1969.

[3] M. Meisel, "Supersolid ^{4}He: an overview of past searches and future possibilities," *Physica B,* vol. 178, pp. 121-128, 1992.

[4] A. Andrreev, K. Keshishev, L. Meezhov-Deglin and A. Shal'nikov, "Attempt at Observing Vacancions In ^{4}He Cyrstals," *Sov. Phys. JETP lett.,* vol. 9, p. 306, 1969.

[5] G. A. Armstrong, A. A. Helmy and A. S. Greenberg, "Boundary-limited thermal conductivity of hcp ^{4}He," *Physical Revew B,* vol. 20, p. 1061–1064 , 1979.

[6] A. J. Legget, "Can a Solid Be "Superfluid"?," *Physical Review Letters,* vol. 25, p. 1543, 1970.

[7] D. J. Bishop, M. A. Paalanen and J. D. Reppy, "Search for superfluidity in hcp ^{4}He," *Physical Review B,* vol. 24, pp. 2844-2845, 1981.

[8] J. M. Goodkind, "Interaction of First and Second Sound in Solid ^{4}He: Properties of a Possible Bose Condensate," *Physical Revew Letters,* vol. 89, p. 095301, 2002.

[9] P.-C. Ho, I. Bindloss and J. Goodkind, "A New Anomaly in solid ^{4}He," *Journal of Low Temperature Physics,* vol. 109, pp. 409-421, 1997.

[10] E. Kim and M. H. W. Chan, "Probable observation of a supersolid helium phase," *Nature ,* vol. 427, pp. 225-227, 2004.

[11] E. Kim and M. H. W. Chan, "Observation of Superflow in Solid Helium," *Science,* vol. 305, pp. 1941 - 1944, 2004.

[12] A. Rittner and J. Reppy, "Disorder and the Supersolid State of Solid ^{4}He," *Phisical Review Letters,* vol. 98, p. 175302, 2007.

[13] E. Kim, J. S. Xia, J. T. West, X. Lin, A. Clark and M. H. W. Chan, "Effect of ^{3}He Impurities on the Nonclasical Response to Oscilation of Solid ^{4}He," *Physical Review Letters,* vol. 100, p. 065301, 2008.

[14] Y. Aoki, J. C. Graves and H. Kojima, "Oscillation Frequency Dependence of Nonclassical Rotation Inertia of Solid ^{4}He," *Physical Review Letters,* vol. 99, p. 015301, 2007.

[15] J. R. Davis, "Heat Treating of Beryllium-Copper Alloys," in *Copper and Copper Alloys*, ASM International, 2001, pp. 253-257.

[16] R. C. Richardson and E. N. Smith, Experimental techneques in condensed matter physics at low temperatures, Addison wesley publishing company, Inc., 1988.

[17] RV-Elektroniikka Oy Picowatt, "PICOWATT - AVS-47 AC Resistance Bridge," 08 March 2014. [Online]. Available: http://www.picowatt.fi/avs47/avs47.html.

[18] D. S. Greywall and P. A. Busch, "^{3}He-melting-curve thermometry," *Journal of Low Temperature Physics,* vol. 46, no. 5-6, pp. 451-465, 1982.

[19] E. D. Adams and R. A. Scribner, "Use of the ^{3}He Melting Curve for Low Temperature Thermometry," *Review of Scientific Instruments,* vol. 41, no. 2, p. 287, 1970.

[20] B. S. James and R. J. Donnelly, "The calculated thermodynamic properties of superfluid ^{4}He," *Journal of Physical and Chemical Reference Data,* vol. 6, pp. 51-104, 1977.

[21] P. Gumann, M. Keiderling, D. Ruffner and H. Kojima, "Effects of He 3 impurity on solid He 4 studied by compound torsional oscillator," *Physical Review B,* vol. 83, no. 22, p. 224519, 2011.

[22] P. Gumann, D. Ruffner, M. Keiderling and H. Kojima, "Effects of ^{3}He Impurity on the Non-classical Rotational Inertia of Solid ^{4}He Studied by Double Resonance Torsional Oscillator," *Journal of Low Temperature Physics,* vol. 158, no. 3-4, pp. 567-571, 2010.

[23] Z. Nussinov, A. V. Balatsky, M. J. Graf and S. A. Trugman, "Origin of the decrease in the torsional-oscillator period of solid ^{4}He," *Phys. Rev. B,* vol. 76, p. 014530, 2007.

[24] M. Graff, Z. Nussinov and A. Balatsky, "The Glassy Response of Solid ^{4}He to Torsional Oscillations," *Journal of Low Temperature Physics,* vol. 158, p. 550, 2010.

[25] I. Iwasa, "Dislocation-vibration model for nonclassical rotational inertia," *Physical review B,* vol. 81, p. 104527, 2010.

[26] P. Gumann, M. Keiderling and H. Kojima, "Hysteretic Response of Torsionally Oscillated Solid ^{4}He and Its Dependence on ^{3}He Impurity Concentration," *Journal of Low Temperature Physics,* vol. 168, no. 3-4, pp. 162-174, 2012.

[27] P. Anderson, "Two new vortex liquids," *Nature Physics,* vol. 3, pp. 160 - 162, 2007.

[28] J. Day and J. Beamish, "Low-temperature shear modulus changes in solid ^{4}He and connection to supersolidity," *Nature,* vol. 450, pp. 853-856, 2007.

[29] A. C. Clark, J. D. Maynard and M. H. W. Chan, "Thermal history of solid ^{4}He under oscillation," *Physical Review B,* vol. 77, p. 184513, 2008.

[30] D. Y. Kim and M. H. W. Chan, "Absence of Supersolidity in Solid Helium in Porous Vycor Glass," *Physical Revew Letters,* vol. 109, p. 155301, 2012.